International Journal of Photoenergy

Photocatalytic Nanomaterials for Energy Conversion and Storage

Lead Guest Editor: Hao Li
Guest Editors: Zhao Ding, Houyang Chen, and Shaoyuan Liu

Photocatalytic Nanomaterials for Energy Conversion and Storage

International Journal of Photoenergy

Photocatalytic Nanomaterials for Energy Conversion and Storage

Lead Guest Editor: Hao Li
Guest Editors: Zhao Ding, Houyang Chen, and Shaoyuan Liu

Chief Editor

Academic Editors

Contents

Hindawi
International Journal of Photoenergy
Volume 2020, Article ID 8870194, 8 pages
https://doi.org/10.1155/2020/8870194

Research Article

Shift the Photocatalytic Activity of P25 TiO_2 Nanoparticles toward the Visible Region upon Surface Modification with Organic Hybrid of Phosphotungstate

Mehdi Taghdiri[1,2] **and Shahrban Dadari Doolabi**[1]

[1]*Department of Chemistry, Payame Noor University, 19395-3697 Tehran, Iran*
[2]*Research Center of Environmental Chemistry, Payame Noor University, Ardakan, Yazd, Iran*

Correspondence should be addressed to Mehdi Taghdiri; mehditaghdiri@yahoo.com

Received 2 August 2020; Revised 30 September 2020; Accepted 12 October 2020; Published 2 November 2020

Academic Editor: Hao Li

In this study, a visible-light-driven P25 TiO_2 was prepared upon surface modification with a colored organic hybrid of phosphotungstic acid that makes titanium dioxide suitable for photocatalytic degradation of organic pollutants under visible and sunlight irradiation. Visible shifting of the photocatalytic activity of surface-modified TiO_2 was examined by studying the decolorization of methylene blue (MB) and rhodamine B (RhB). The results show that colored TiO_2 is, unlike bare TiO_2, a good photocatalyst in the degradation of dyes under visible and sunlight irradiation. Surface-modified Al_2O_3 and reduced graphene oxide (RGO) with organic hybrid of phosphotungstate failed to degrade RhB under sunlight irradiation, which prove the role of TiO_2 in the photochemical process.

1. Introduction

The major limitation of P25 TiO_2 as a photocatalyst is its poor efficiency in the visible region of the solar spectrum due to wide band gap of 3.2 eV, which typically requires exposure of ultraviolet (UV) light for photocatalytic reactions. Hence, the photocatalytic application of TiO_2 at an industrial scale has been limited because only 4-5% of the solar spectrum corresponds to UV photons. Therefore, strong efforts have been devoted to activating the TiO_2 toward the visible and solar light for application purposes [1, 2]. One of the approaches for attainment of this issue is dye sensitization, i.e., the adsorption of dyes especially phthalocyanines on the TiO_2 surface [3–8]. One other is modification with polyoxometalates (POMs), but pure POMs cannot shift the photocatalytic activity of pure P25 TiO_2 toward the visible region, and it is necessary to join them to valuable metallic or nonmetallic moieties [9–13]. In this work and in the following of our previous works [14, 15], we have utilized the combination of dye sensitization and POMs, i.e., the adsorbed MB on phosphotungstate-hexamethylenetetramine hybrid (PTA-HMT-MB) as sensitizer. To our knowledge, the coating of P25 TiO_2 with a colored organic hybrid of POMs has not been reported yet. The hybridization and immobilization onto P25 TiO_2 resolve high solubility and poor recyclability of POMs and facilitate separation because coated TiO_2 is not suspended in the solution.

2. Experimental

2.1. Chemicals and Reagents. The P25 TiO_2 was from Plasma-Chem GmbH (Berlin, Germany) with the nominal 21 ± 10 nm particle size, and the phosphotungstic acid hydrate ($H_3PW_{12}O_{40}{\cdot}xH_2O$, total impurities < 0.06%) was from Fluka. The hexamethylenetetramine (HMT) ($C_6H_{12}N_4$, 99.5%) was from Sina Chemical Industries Co. (Shiraz, Iran). Activated alumina (Al_2O_3) and reduced graphene oxide (RGO) were

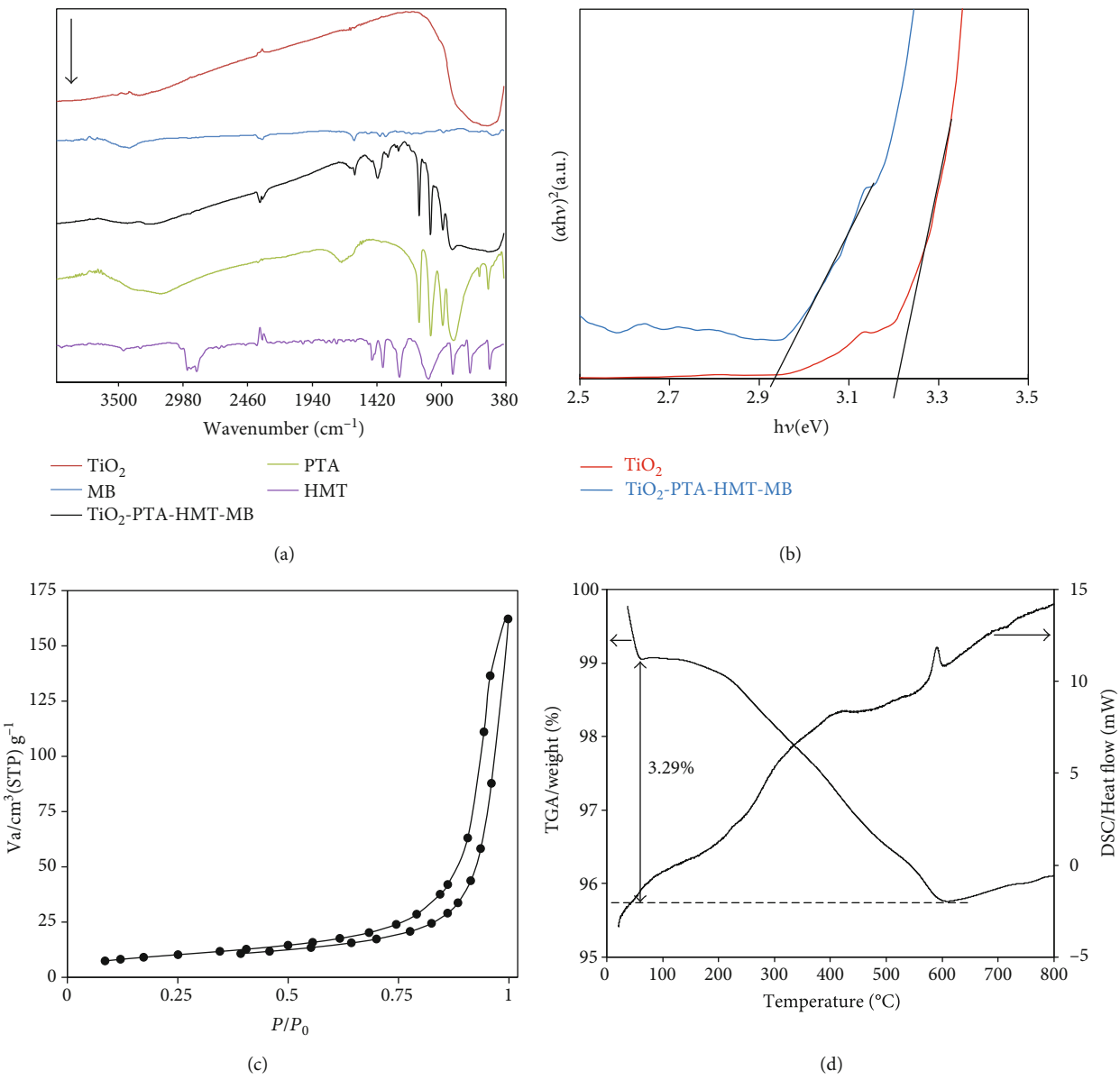

Figure 1: (a) FTIR spectra, (b) Tauc's plots of TiO_2 and TiO_2-PTA-HMT-MB for determining the band gap energy from variation of $(\alpha h\nu)^2$ with photon energy ($h\nu$), (c) N_2 adsorption-desorption isotherm, and (d) TGA and DSC curves of TiO_2-PTA-HMT-MB.

consigned by Ardakan Industrial Ceramics Co. (Ardakan, Iran) and Nanostructured Coatings Institute (Yazd, Iran), respectively. Other reagents were purchased from commercial sources and used without further purification.

2.2. Apparatus. The stirring of solutions was performed using a Labinco magnetic stirrer model L-81. A Metrohm type 691 pH meter was used for pH measurements. UV-Vis absorption spectra were obtained using a GBC model Cintra 6 or Shimadzu 1601PC spectrophotometer. The IR spectra were conducted on a Shimadzu 8400s FTIR spectrometer. Diffuse reflectance spectra (DRS) were recorded on an Avantes spectrometer (AvaSpec-2048-TEC), using $BaSO_4$ as a standard. The surface area and pore volume of the composite were measured and calculated by the BET method from nitrogen adsorption-desorption isotherms at 77 K with a surface area and pore size analyzer (BELSORP-mini II, Bel, Japan). The thermogravimetric analysis (TGA) and differential scanning calorimetry (DSC) were performed on a Rheometric Scientific STA 1500 thermal analyzer under the atmosphere of air. Scanning electron microscopy (SEM) and transmission

Table 1: Textural parameters of the P25 TiO_2 and TiO_2-PTA-HMT-MB composite.

Sample	Surface area (m^2/g)	Mean pore diameter (nm)	Total pore volume (cm^3g^{-1})
P25 TiO_2	56.191	18.062	0.2537
TiO_2-PTA-HMT-MB	28.372	31.795	0.2255

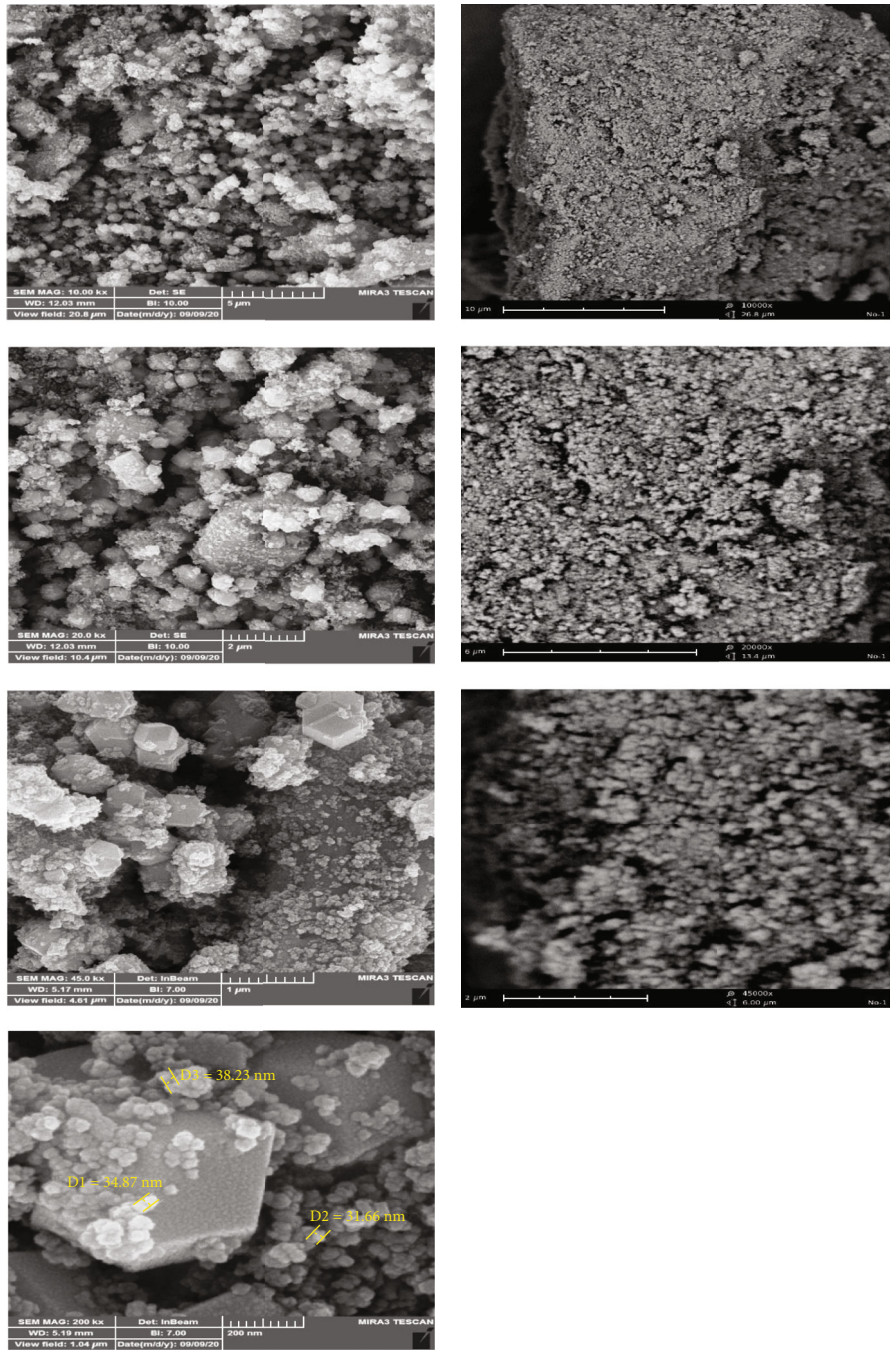

(a) (b)

Figure 2: SEM images of TiO_2-PTA-HMT-MB (a) and TiO_2 (b) at magnifications of 10000, 20000, 45000, and 200000 (from top to down).

electron microscopy (TEM) for TiO_2-PTA-HMT-MB were performed using FESEM TESCAN MIRA3 and TEM Philips EM 208S, respectively.

2.3. Preparation of Composites. The TiO_2-PTA-HMT-MB composite was prepared in two steps. In the first step, the PTA-HMT was prepared according to our previous works [15, 16]. 10 mL hexamethylenetetramine aqueous solution (1.0% *w*/*w*) was mixed with a 10 mL phosphotungstic acid aqueous solution (7.5% *w*/*w*). The immediate result was a milky suspension, which was magnetically stirred at 500 rpm for 3 h at an ambient temperature. Then, the white precipitate was filtered, washed with distilled water, and dried at 100°C. In the second step, the modified P25 TiO_2 nanopowder, i.e., TiO_2-PTA-HMT-MB, was obtained by adding 0.195 g PTA-HMT to 50 mL MB solution (134 mg L^{-1}), and the pH of the mixture reached 2.5. Then, 0.195 g P25 TiO_2 was added to it, and the solution was stirred for 6 h. At the end, the precipitate was filtered and dried in an oven for 3 h, at 100°C. The Al_2O_3-PTA-HMT-MB and

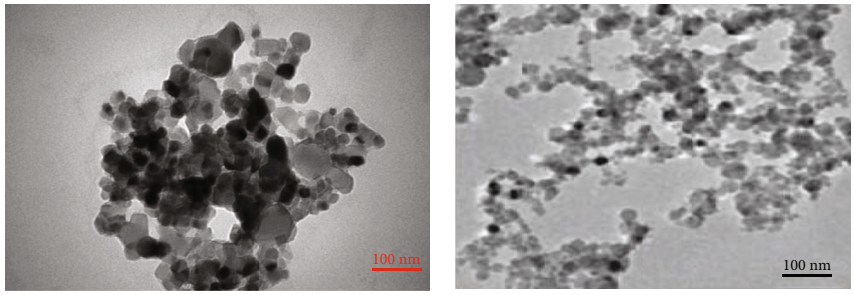

(a) (b)

Figure 3: TEM image of TiO_2-PTA-HMT-MB (a) and P25 TiO_2 (b).

RGO-PTA-HMT-MB composites were prepared similar to the above manner.

2.4. Evaluation of the Photocatalytic Activity. Solar photocatalytic experiments were performed similar to our previous works [14, 15]. 100 mL RhB (15 mg L^{-1}) and a specific amount of the photocatalyst were transferred to a beaker, capped by cellophane, and exposed to sunlight in September 2017 between 11 am and 3 pm at the Payame Noor University, Ardakan, Yazd, Iran (GPS coordinates: 32°29′N, 53°59′E). The experiments were conducted without stirring during solar irradiation. The visible light experiments were carried out using a metal halide lamp (500 W, Philips). 15 mL MB solutions (30 mg L^{-1}) and a predetermined amount of the photocatalyst were transferred to a 200 mL water-cooled cylindrical Pyrex vessel reactor. The distance between the reactor and the light source was 10 cm. The radiation intensity is about 900 W/m^2 [17]. The reaction was started by switching on the light source after adding the composite to the dye solutions. The reactor was placed on a magnetic stirrer and stirred continuously. Temperature of the reactor was maintained at 27°C by considering a cooling chamber around the reactor and circulating water in it. During two processes, at given time intervals, 4 mL of suspension was withdrawn, and the composite was removed and then analyzed by a UV-Vis spectrophotometer. The C/C_0 values were obtained through the maximum absorption in the whole absorption spectrum in order to plot C/C_0 vs. time curves.

3. Results and Discussion

3.1. Characterizations. The IR spectrum of TiO_2-PTA-HMT-MB exhibits the characteristic bands of the HMT and MB organic moieties and of TiO_2 and PTA inorganic moieties (Figure 1(a)). The band positioned at 555 cm^{-1} refers to the symmetric stretching of TiO_2. The strong absorption peaks at 1100-750 cm^{-1} show the presence of $PW_{12}O_{40}^{3-}$ anions with the α-Keggin structure. The 887 cm^{-1} band is related to the W-O_b-W stretching mode of PTA while the 987 cm^{-1} band corresponds to its W-O_d scissoring mode. The peak about 1250 cm^{-1} can be attributed to the vibration of the CH_2 of HMT [18], and the 1597 cm^{-1} corresponds to the vibration of the aromatic ring of MB [19]. The band gaps of TiO_2 and TiO_2-PTA-HMT-MB were determined from the diffuse reflectance spectra using Tauc's plots (Figure 1(b)). It is clear that there are differences in the band gap values of TiO_2 and modified TiO_2. The band gap of TiO_2-PTA-HMT-MB (2.94 eV) has been shifted to the visible region (422 nm) in comparison with the band gap of TiO_2 (3.2 eV, 388 nm). To determine the specific surface area, total pore volume and mean pore diameter of the TiO_2-PTA-HMT-MB, BET analysis method, and N_2 adsorption-desorption measurement (Figure 1(c)) were used. The measured specific surface area of the composite was 28.372 m^2/g, which is lower than that of TiO_2 (56.191 m^2/g). Indeed, the pores are loaded by the PTA-HMT-MB hybrid. The mean pore diameter and total pore volume were 31.795 nm and 0.2255 cm^3g^{-1}, respectively. Textural parameters of the P25 TiO_2 and TiO_2-PTA-HMT-MB hybrid are compared in Table 1. According to the IUPAC classification, the mentioned mean pore diameter belongs to the mesopore groups [20]. The TG and DSC curves of the TiO_2-PTA-HMT-MB composite are shown in Figure 1(d). The exothermic peak at 593°C is related to the decomposition of phosphotungstate to WO_3 and P_2O_5. The weight loss of 3.29% is ascribed to the loss of the organic

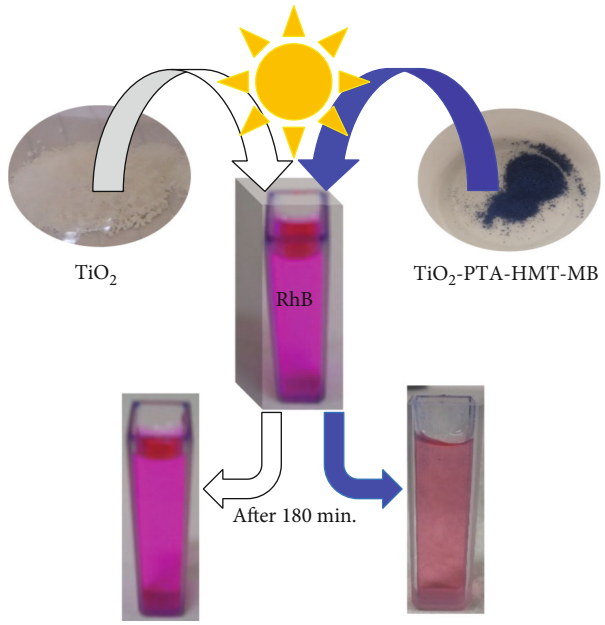

Scheme 1: Schematic illustration of the solar photocatalytic experiment for RhB.

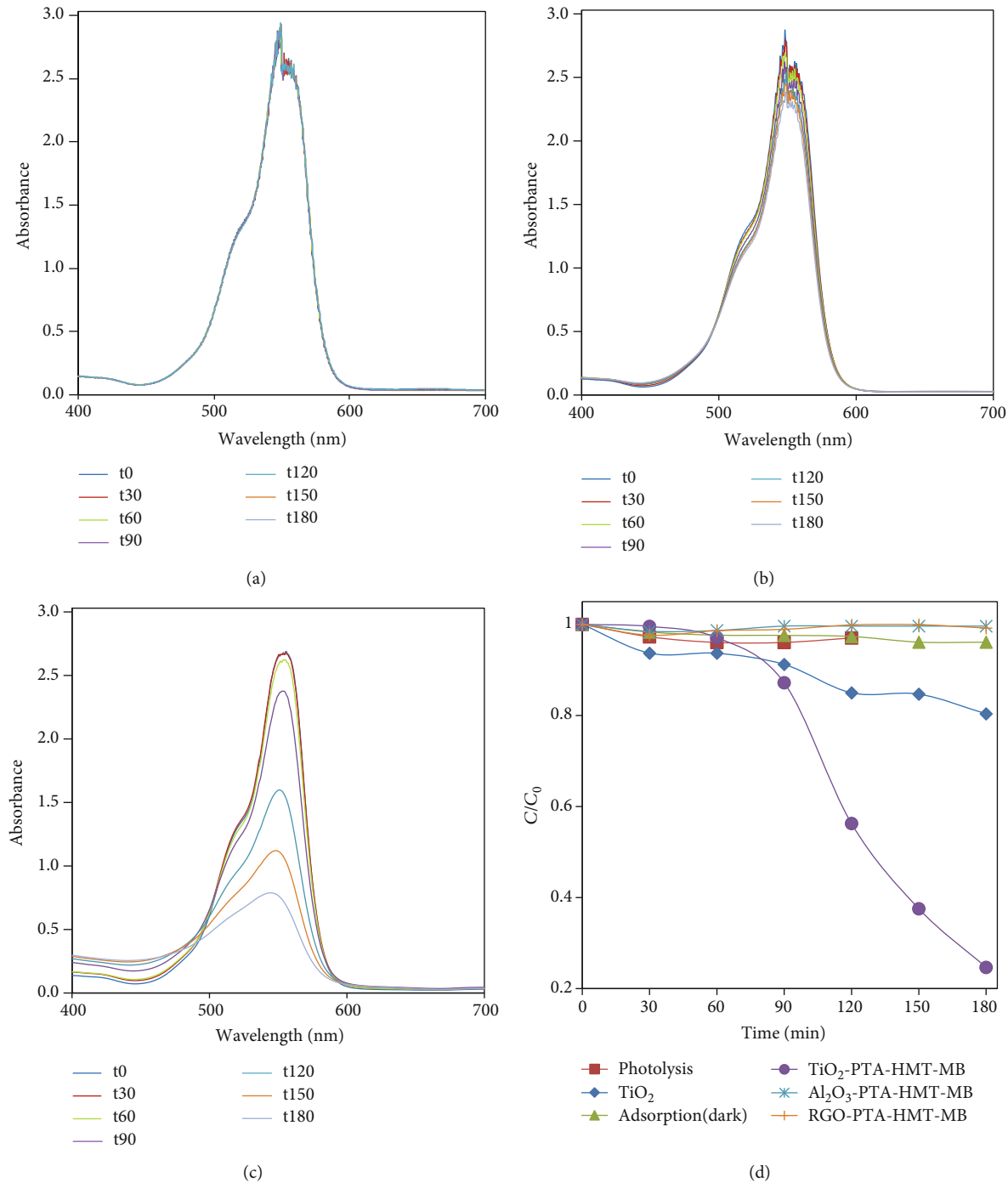

FIGURE 4: UV-Vis absorption spectra of RhB (15 mg/L, 100 mL, pH = 9.0) during the photodegradation under sunlight without photocatalyst (photolysis) (a), in the presence of TiO_2 (0.15 g/L) (b), in the presence of TiO_2-PTA-HMT-MB (0.1 g/L) (c), and C/C_0 vs. time curves (d).

moieties of the composite, i.e., HMT-MB. Figure 2 shows the SEM images of TiO_2-PTA-HMT-MB and TiO_2 nanoparticles. Comparison of these images displays that uniform distribution and neat morphology of TiO_2 nanoparticles are not observed in TiO_2-PTA-HMT-MB nanoparticles. The TEM images in Figure 3 show that modified TiO_2 nanoparticles agglomerated to larger particles with an irregular shape than P25 TiO_2. The sizes of TiO_2-PTA-HMT-MB nanoparticles were estimated from the TEM image in the range of 30–80 nm which are in agreement with the sizes obtained from the SEM image (Figure 2).

3.2. Photocatalytic Degradation of RhB. The composite was applied for photodecomposition of RhB under sunlight irradiation. Schematic illustration of the photocatalytic experiment is shown in Scheme 1. UV-Vis absorption

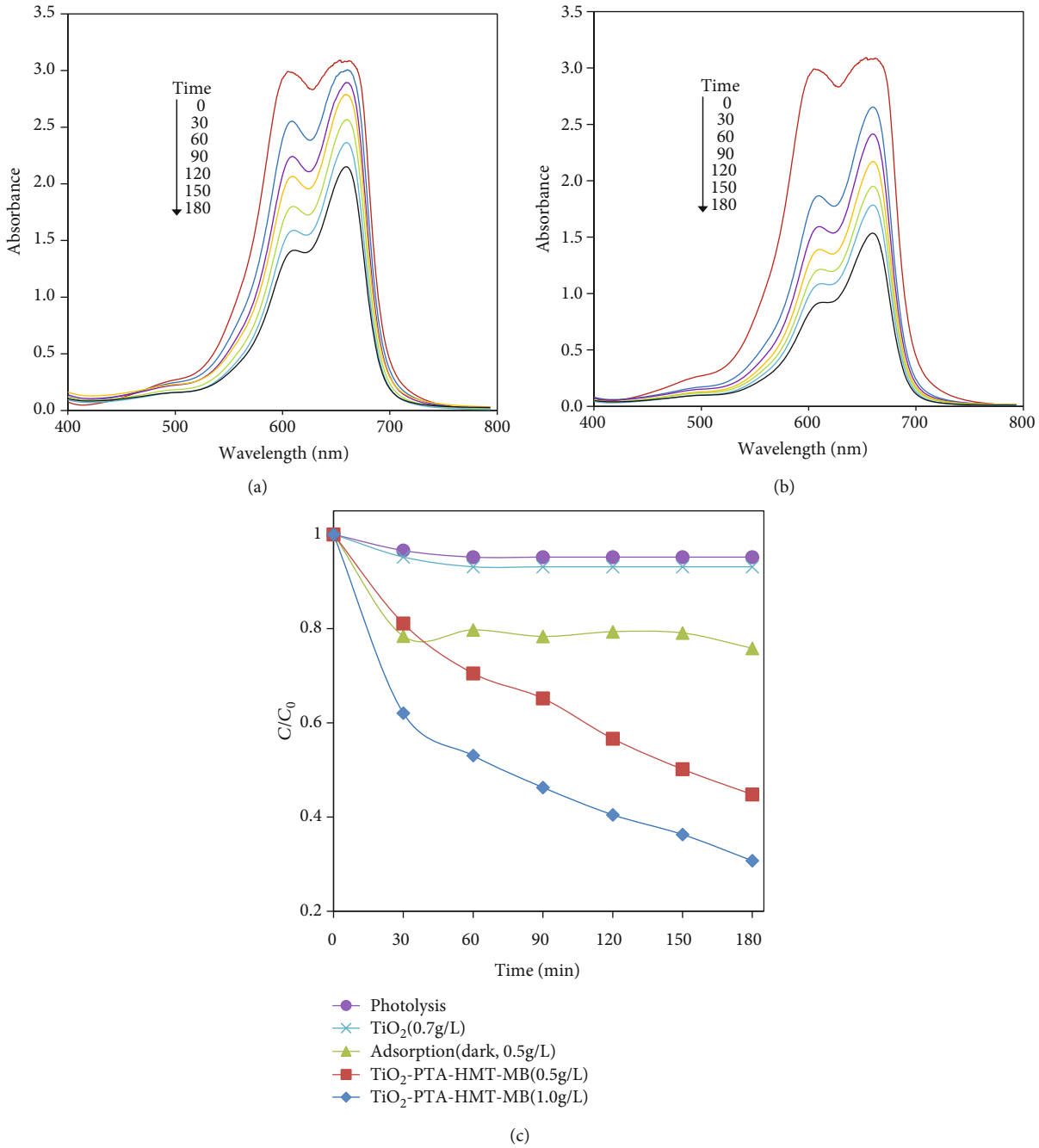

Figure 5: UV-Vis absorption spectra of MB (30 mg/L, pH = without adjustment = 5.7) during the photodegradation under visible light in the presence of TiO_2-PTA-HMT-MB (0.5 g/L) (a), (1.0 g/L) (b), and C/C_0 vs. time curves (c).

spectra of RhB (15 mg/L, 100 mL, pH = 9.0) during the photodegradation under sunlight without photocatalyst (photolysis), in the presence of TiO_2 and modified TiO_2, are shown in Figures 4(a)–4(c). TiO_2-PTA-HMT-MB cannot adsorb RhB because RhB ($pK_a = 3.1$) is in neutral form at pH 9.0 (Figure 4(d)). The photodegradation of RhB is negligible due to photolysis and in the presence of TiO_2 (0.15 g/L) (Figure 4(d)). However, it becomes noticeable in the presence of TiO_2-PTA-HMT-MB (0.1 g/L) that is an indicative shift in the photocatalytic activity of P25 TiO_2 nanoparticles toward the visible region upon surface modification with phosphotungstate hybrid. The composites of Al_2O_3-PTA-HMT-MB and RGO-PTA-HMT-MB failed to degrade RhB under sunlight irradiation (Figure 4(d)), which prove the role of TiO_2 in the photochemical process. Indeed, an excited surface-adsorbed hybrid (PTA-HMT-MB) injects a charge into the conduction band of TiO_2, and then reactive radicals are produced and degrade RhB.

3.3. Photocatalytic Degradation of MB. The composite was then tested as a catalyst for the photocatalytic degradation

Table 2: Comparison of photodegradation of dyes by using TiO_2-PTA-HMT-MB and reported P25 TiO_2-POMs.

Catalysts	Light	C_{dye} (mg/L)	Catalyst dosage (g/L)	Time (min)	Decolorization (%)	Ref.
$TiW_{11}Ti/TiO_2$	UV	Brilliant dye X-3B (40)	0.59	20	97.4	[22]
$HP_{62}W_{18}O_{62}/TiO_2/\beta$-zeolite	UV	MO (16)	1.4	180	65[a]	[23]
Fe-PTA/P25	Simulated sunlight	MB (20)	50 mg + 50 mmol H_2O_2[b]	12	47[a]	[24]
P25-PEI-$P_2Mo_{15}V_3$	Simulated sunlight	MB (40)	0.25	115	75[a]	[25]
P25 TiO_2-PTA-HMT-MB	Sunlight	RhB (15)	0.1	180	75.3	This work
P25 TiO_2-PTA-HMT-MB	Vis.	MB (30)	1.0	180	69.3	This work

[a]Value was estimated from original figure of the reference; [b]volume of solution is unknown. Note: PEI: polyethyleneimine; MO: methyl orange.

of MB under visible light. While the P25 TiO_2 (0.7 g/L) shows very low photocatalytic activity toward MB degradation, the TiO_2-PTA-HMT-MB is very active (Figure 5). The photodegradation without photocatalyst (photolysis) and the removal of MB due to adsorption on the composite were evaluated in order to indicate the performance of the TiO_2-PTA-HMT-MB photocatalyst (Figure 5(c)).

3.4. Comparison with Other P25 TiO_2-POM Composites. Until now, many studies have been conducted in order to modify titanium dioxide [1, 21], but the majority have used the sol-gel method not P25 TiO_2. The photocatalytic efficiency of the TiO_2-PTA-HMT-MB composite is compared with other P25 TiO_2-POM composites in Table 2. It should be noted that the light sources are visible light and sunlight in this work while these are UV light and simulated sunlight in other works. As it is seen, the combination of P25 TiO_2 with lone POMs such as $TiW_{11}Ti$ [22] and $HP_{62}W_{18}O_{62}$ [23] does not shift the photocatalytic activity to visible light. However, this purpose has been achieved by the incorporation of a third component together with POMs such as Fe [24], polyethyleneimine [25], and HMT-MB (this work). The findings show that the advantage of the present photocatalyst is the shift of the photocatalytic activity toward the visible region, and hence, it shows the photocatalytic behavior under a visible light source (metal halide lamp) in addition to sunlight.

4. Conclusion

In summary, P25 TiO_2 was coated with PTA-HMT-MB hybrid. The TiO_2-PTA-HMT-MB composite indicated a narrower band gap than P25 TiO_2. The photocatalytic performance was evaluated by the photodegradation of RhB and MB under solar and visible light, respectively. The decolorization of these dyes with pure P25 TiO_2 in the solar/visible light is negligible while the POM hybrid coating causes decolorization with TiO_2-PTA-HMT-MB to be remarkable. This work presents the incorporation of an organic hybrid of phosphotungstate as an effective strategy for exploration of shifting the photocatalytic activity of P25 TiO_2 toward the visible region, thereby facilitating the solar light driven photocatalysis.

Data Availability

The readers can access the supporting data through contact with the corresponding author.

Conflicts of Interest

The authors declare that there is no conflict of interest regarding the publication of this paper.

Acknowledgments

This work was supported by Payame Noor University. The authors express their appreciation for support of this study.

References

[1] M. Humayun, F. Raziq, A. Khan, and W. Luo, "Modification strategies of TiO_2 for potential applications in photocatalysis: a critical review," *Green Chemistry Letters and Reviews*, vol. 11, no. 2, pp. 86–102, 2018.

[2] Y. Liu, J.-F. Wan, C.-T. Liu, and Y.-B. Li, "Fabrication of magnetic $Fe_3O_4/C/TiO_2$ composites with nanotube structure and enhanced photocatalytic activity," *Materials Science and Technology*, vol. 32, no. 8, pp. 786–793, 2016.

[3] D. Chatterjee and A. Mahata, "Visible light induced photodegradation of organic pollutants on dye adsorbed TiO_2 surface," *Journal of Photochemistry and Photobiology A: Chemistry*, vol. 153, no. 1-3, pp. 199–204, 2002.

[4] S. Xu, W. Lu, S. Chen et al., "Colored TiO_2 composites embedded on fabrics as photocatalysts: Decontamination of formaldehyde and deactivation of bacteria in water and air," *Chemical Engineering Journal*, vol. 375, article 121949, 2019.

[5] V. Iliev, "Phthalocyanine-modified titania—catalyst for photooxidation of phenols by irradiation with visible light," *Journal of Photochemistry and Photobiology A: Chemistry*, vol. 151, no. 1-3, pp. 195–199, 2002.

[6] A. Ebrahimian, M. A. Zanjanchi, H. Noei, M. Arvand, and Y. Wang, "TiO_2 nanoparticles containing sulphonated cobalt phthalocyanine: Preparation, characterization and photocatalytic performance," *Journal of Environmental Chemical Engineering*, vol. 2, no. 1, pp. 484–494, 2014.

[7] E. Vargas, R. Vargas, and O. Núñez, "A TiO_2 surface modified with copper (II) phthalocyanine-tetrasulfonic acid tetrasodium salt as a catalyst during photoinduced dichlorvos mineralization by visible solar light," *Applied Catalysis B: Environmental*, vol. 156-157, pp. 8–14, 2014.

[8] W. A. V. Lozada, C. Diaz-Uribe, C. Quiñones, M. Lerma, C. Fajardo, and K. Navarro, "Phthalocyanines: alternative sensitizers of TiO_2 to be used in photocatalysis," *Phthalocyanines and Some Current Applications*, vol. 223, 2017.

[9] S. J. Chen, Q. Gan, H. R. Shang, and X. Liu, "Preparation and characterization of $H_3PW_{12}O_{40}/TiO_2$-M (M=Fe, Co, Ni, Zn) and photocatalytic activity for methyl orange decomposition," *Advanced Materials Research*, vol. 1073-1076, pp. 202–209, 2014.

[10] A. Pearson, S. K. Bhargava, and V. Bansal, "UV-switchable polyoxometalate sandwiched between TiO_2 and metal nanoparticles for enhanced visible and solar light photococatalysis," *Langmuir*, vol. 27, no. 15, pp. 9245–9252, 2011.

[11] H. Shi, Y. Yu, Y. Zhang et al., "Polyoxometalate/TiO_2/Ag composite nanofibers with enhanced photocatalytic performance under visible light," *Applied Catalysis B: Environmental*, vol. 221, pp. 280–289, 2018.

[12] H. Shi, T. Zhao, Y. Zhang et al., "Pt/POMs/TiO_2 composite nanofibers with an enhanced visible-light photocatalytic performance for environmental remediation," *Dalton Transactions*, vol. 48, no. 35, pp. 13353–13359, 2019.

[13] L. Li, L. Li, T. Sun et al., "Novel $H_3PW_{12}O_{40}/TiO_2$-g-C_3N_4 type-II heterojunction photocatalyst with enhanced visible-light photocatalytic properties," *Journal of Solid State Chemistry*, vol. 274, pp. 152–161, 2019.

[14] M. Taghdiri, "Selective adsorption and photocatalytic degradation of dyes using polyoxometalate hybrid supported on magnetic activated carbon nanoparticles under sunlight, visible, and UV irradiation," *International Journal of Photoenergy*, vol. 2017, Article ID 8575096, 15 pages, 2017.

[15] M. Taghdiri and S. Dadari Doolabi, "Visible/solar-light driving photocatalytic activity of TiO_2 nanotubes upon coating with phosphotungstate hybrid," *International Journal of Environmental Analytical Chemistry*, pp. 1–17, 2020.

[16] H. Mirhoseini and M. Taghdiri, "Extractive oxidation desulfurization of sulfur-containing model fuel using hexamine–phosphotungstate hybrid as effective heterogeneous catalyst," *Fuel*, vol. 167, pp. 60–67, 2016.

[17] H. Moria, T. Mohamad, and F. Aldawi, "Radiation distribution uniformization by optimized halogen lamps arrangement for a solar simulator," *Journal of Scientific and Engineering Research*, vol. 3, pp. 29–34, 2016.

[18] J. O. Jensen, "Vibrational frequencies and structural determinations of hexamethylenetetraamine," *Spectrochimica Acta Part A: Molecular and Biomolecular Spectroscopy*, vol. 58, no. 7, pp. 1347–1364, 2002.

[19] H. Yao, N. Li, S. Xu, J. Xu, J. Zhu, and H. Chen, "Electrochemical study of a new methylene blue/silicon oxide nanocomposition mediator and its application for stable biosensor of hydrogen peroxide," *Biosensors & Bioelectronics*, vol. 21, no. 2, pp. 372–377, 2005.

[20] R. Francoise and R. Jean, *Adsorption by Powders and Porous Solids; Principles*, Methodology and Applications, in, Academic Press, London, 1999.

[21] M. Pelaez, N. T. Nolan, S. C. Pillai et al., "A review on the visible light active titanium dioxide photocatalysts for environmental applications," *Applied Catalysis B: Environmental*, vol. 125, pp. 331–349, 2012.

[22] L. Ai, D. Zhang, Q. Wang, F. He, H. Yang, and Q. Wu, "Preparation of Ti-heteropolyacid/TiO_2 and its rapid photocatalytic degradation of X-3B," *Journal of Materials Science: Materials in Electronics*, vol. 31, no. 4, pp. 3166–3171, 2020.

[23] M. Moosavifar and S. Bagheri, "Photocatalytic performance of $H_6P_2W_{18}O_{62}/TiO_2$Nanocomposite encapsulated into beta zeolite under UV irradiation in the degradation of methyl orange," *Photochemistry and Photobiology*, vol. 95, no. 2, pp. 532–542, 2018.

[24] X. An, Q. Tang, H. Lan, H. Liu, and J. Qu, "Polyoxometalates/-TiO_2 Fenton-like photocatalysts with rearranged oxygen vacancies for enhanced synergetic degradation," *Applied Catalysis B: Environmental*, vol. 244, pp. 407–413, 2019.

[25] J. Zhang, W.-L. Chen, and E.-B. Wang, "Synthesis and catalytic properties of novel POM@TiO_2 composite materials," *Inorganic Chemistry Communications*, vol. 38, pp. 96–99, 2013.

Hindawi
International Journal of Photoenergy
Volume 2020, Article ID 8897667, 14 pages
https://doi.org/10.1155/2020/8897667

Research Article

Facile Preparation of ZnO Nanoparticles and Ag/ZnO Nanocomposite and Their Photocatalytic Activities under Visible Light

Thi Anh Tuyet Pham,[1] Van Anh Tran,[1] Van Duong Le,[1] Minh Viet Nguyen,[2] Duc Duc Truong,[1] Xuan Truong Do,[1] and Anh-Tuan Vu[1]

[1]*School of Chemical Engineering, Hanoi University of Science and Technology, Hanoi, Vietnam*
[2]*Faculty of Chemical Engineering, Hanoi University of Industry, Vietnam*

Correspondence should be addressed to Anh-Tuan Vu; tuan.vuanh@hust.edu.vn

Received 11 August 2020; Revised 10 September 2020; Accepted 7 October 2020; Published 22 October 2020

Academic Editor: Hao Li

Zinc oxide (ZnO) has been known as an excellent photocatalyst for the degradation of a variety of organic pollutants under UV irradiation. This work describes a synthesis of ZnO nanoparticles via a facile precipitation method, and Ag was doped into Ag/ZnO nanocomposite to improve the photocatalytic degradation of BPA under visible light irradiation. The obtained ZnO nanoparticles were 20 nm in size and had a relatively high surface area and pore volume, 26.2 m^2/g and 0.48 cm^3/g, respectively. The deposition of Ag led to a decrease in the surface area, pore volume, and band gap energy (E_g) of ZnO nanoparticles. However, the photocatalytic activity of Ag/ZnO composite in the case increased. The performance of ZnO was compared with Ag/ZnO composites at the different molar ratios, and the kinetic reaction of BPA in these catalysts was investigated by the first-order kinetic model. The sample of Ag/ZnO-10 composite had the highest catalytic activity and showed the degradation efficiency, reaction rate, and degradation capacity of 100% in 120 min, 0.014 min^{-1}, and 40 mg/g, respectively. In comparison, the effects of Ag/ZnO molar ratio, catalyst dosage, solution pH, and concentration of BPA on photocatalytic degradation were investigated. Additionally, the photocatalytic performance of Ag/ZnO-10 composite was evaluated by the degradation of other persistent organic compounds such as phenol, tartrazine, and methylene blue and compared to other catalysts in literature.

1. Introduction

Today, significant development of inorganic nanoparticles has been their potential application in the environment, biology, electronics, optics, transport, and information technology [1]. That is reflected in the exponential increase in the number of scientific reports, patents, and companies related to science and nanotechnology, in which semiconductor technology from inorganic nanoparticles as the photocatalysts for environmental remediation has been widely studied. Zinc oxide (ZnO) is one of the commonly used semiconductors, with a wide band gap at room temperature (3.27 eV), the linear electronic displacement, and a large exciton binding energy (around 60 meV) [2]. In comparison to other oxide semiconductors, ZnO has many superior properties such as light sensitive, thermal and chemically stable, low cost, nontoxic, and sustainable with hydrogen environment [3]. The ZnO-based materials have many applications in industries, for example, rubbers, ceramics, pharmaceuticals, agricultural servants, paints, cosmetics, and photocatalysts [4–10]. Besides the advantages of this material due to the high electron aperture rate and low charge separation efficiency [11], the pure ZnO often exhibits relatively low photocatalytic activity under visible light irradiation, and therefore, ZnO does not meet the requirements of a photocatalyst when applied to practical processes [3, 12, 13]. That is why the enhanced catalytic activity of ZnO in visible light by doping other elements is a great concern to scientists.

To this moment, the ZnO nanomaterials with different shapes and sizes have been prepared by many methods such

as hydrothermal, emulsion, chemical vaporization, and combustion methods [14–17]. Each method has its advantages and limitations. The hydrothermal method encounters a difficulty to adjust the shape of the material, and the obtained ZnO is often the rode and plate shapes; in the emulsion methods usually toxic solvents are used; the chemical evaporation method has a low efficiency leading to the high cost of materials; the combustion method faces difficulty in adjusting the particle sizes [18]. Therefore, a facile method for producing ZnO having high production and small particle sizes, at the same time an improved photocatalytic activity, is a crucial aspect for practical applications.

BPA (2,2-bis(4-hydroxyphenyl)propane) is chosen to be the starting material for many synthetic plastics, mainly some polycarbonates and epoxy resins, as well as certain polysulfones and certain suitable materials because BPA-based plastics are strong and tough. It is used in many popular consumer goods, such as plastic bottles, sports equipment, lining of water pipes, CDs, and DVDs [19]. About 4 million tons of BPA chemicals are produced every year to produce polycarbonates, which makes BPA one of the most produced chemicals worldwide. BPA is suspected of being contaminated with food (soluble in food) and has negative health effects such as changes in immune function, cardiovascular disorders, cancer, and infertility [20–23]. It can be found in natural water as a consequence of untreated industrial effluent, and it is very dangerous in the aquatic ecosystem due to its role as an estrogen receptor agonist [24]. According to the current U.S. Environmental Protection Agency standard evaluation procedures, Bisphenol A was moderately to slightly toxic to the fish and invertebrates tested, with LC50 or EC50 values from 1.1 to 10 mg/L. These data did not trigger freshwater or saltwater chronic tests [22]. Therefore, it is imperative and urgent to find a method to remove BPA from contaminated water.

Over the past decades, the treatment of BPA in the environment has been studied using many different approaches. Various technologies have been tested to remove BPA from wastewater like adsorption [25, 26], reverse osmosis [27], mechanical method [28], advanced oxidation processes by Fenton system [29], and photodegradation [30–32]. However, due to its eco-friendly operations, which do not create byproducts in the process, photodegradation has been preferred and extensively used. When a photocatalyst absorbs light irradiation for generating charge carriers and shifting electrons from the valence band (VB) to the conduction band (CB), photodegradation reaction occurs on its active surface through the formation of $^{\cdot}OH$ and $^{\cdot}O_2^-$, which rapidly breakdown target pollutants into the end products of CO_2 and H_2O [33].

There have been many studies on synthesizing ZnO-based materials to decompose toxic organic substances in wastewater [9, 34–37], in which ZnO/TiO_2 and ZnO/rGO-rGH showed the effective materials of degrading BPA under UV irradiation [38, 39]. However, the use of UV light can affect the ecosystem as well as it is much more expensive than using visible light. Thereby, it is essential to improve the visible light absorption of ZnO by loading noble metal (Au, Ag, Pt, and Ru) [40]. On the other hand, modifying ZnO with noble metal nanoparticles also has attracted attention due to promoting the separation of photogenerated charges in photocatalysts through the formation of Schottky barrier and improving the photocatalytic stability [41, 42]. Among the various noble metal-semiconductor photocatalysts, Ag/ZnO can generate an effective Schottky barrier at the junction interface, supporting electron capture, thereby increasing the separation efficiency of electron-hole pairs and boost visible light harvesting capability.

In this study, a facile precipitation method was used to synthesize ZnO nanomaterials, and then, Ag was doped into Ag/ZnO composite with the different molar ratios. As-synthesized samples were characterized by the X-ray powder diffraction (XRD), the field emission scanning electron microscopy (FE-SEM), the transmission electron microscopy (TEM), the Fourier transform infrared spectroscopy (FTIR), and the UV-Vis diffuse reflectance spectra (DR-UV-Vis). The performance of the catalyst was evaluated by degrading BPA in water under visible light irradiation. The effects of Ag/ZnO molar ratio, a catalyst dosage, concentration of BPA, and solution pH on photocatalytic degradation of BPA were investigated. Ag was doped to enhance the photocatalytic performance of Ag/ZnO composite with the degradation of BPA. The effects of the Ag content, a dosage catalyst, a BPA concentration, and pH solution on degradation efficiency of BPA under visible light irradiation were investigated. The optimal reaction conditions and the photocatalytic performance of Ag/ZnO-10 composite were evaluated by degradation of other persistent organic compounds such as phenol, tartrazine (TA), and methylene blue (MB).

2. Materials and Methods

2.1. Materials. Bisphenol A (99%) was purchased from Sigma-Aldrich. $AgNO_3$ (99.8%), $Zn(NO_3)_2{\cdot}6H_2O$ (99%), hexamethylenetetramine ($C_6H_{12}N_4$, 99%), trisodium citrate ($C_6H_5NaO_7S{\cdot}2H_2O$, 99%), and sodium borohydride ($NaBH_4$, 98%) were obtained from Merck. All reagents were used without any further purification. Distilled water was used throughout all experiments.

2.2. Preparation of ZnO. Nano ZnO modified from the precipitation method in the previous report [3]. Typically, 0.02 mol of $Zn(NO_3)_2{\cdot}6H_2O$, 0.02 mol of hexamethylenetetramine, and 0.01 mol of trisodium citrate were dissolved in 100 mL distilled water; the solution was stirred and heated up to 90°C and then was kept at this temperature for 1 h without stirring. The precipitate was filtered and washed several times with distilled water. The powder was dried at 80°C overnight and calcined at 400°C for 2 h at a heating rate of 1°C/min to obtain nano ZnO.

2.3. Preparation of Nanocomposite Ag/ZnO. Typically, 1 g of ZnO and 0.1052 g of $NaBH_4$ were dissolved in 50 mL of distilled water. An amount of $AgNO_3$ corresponding to a desired molar ratio of Ag/ZnO was added into the solution. In this study, molar ratios of 2, 5, 10, and 10 were selected to investigate the effect of Ag content on photodegradation of BPA. The mixture was stirred for 1 h at 60°C and then

filtered and washed several times with distilled water. The grey powder obtained after drying overnight at 60°C was denoted as Ag/ZnO-x, in which x is the molar ratio of Ag/ZnO.

2.4. Characterization. The crystalline phase of samples was investigated by the X-ray powder diffraction. XRD patterns were obtained by using the Bruker D8 Ax XRD diffractometer (Germany) with Cu Kα irradiation (40 kV, 40 mA). The 2θ ranging from 20 to 80° was selected for analyzing the crystal structure. The morphology and size of the samples were observed by transmission electron microscopy (TEM, JEM-2010). The morphology and size of the samples were observed by field emission scanning electron microscopy (FE-SEM, JEOL-7600F). The chemical composition of the composite was determined by energy dispersive spectrometry (EDS: JEOL-7600F). The textural properties were measured via N_2 adsorption/desorption isotherms using a Micromeritics (Gemini VII analyzer). The Fourier transform infrared spectroscopy (FTIR, Madison, WI, USA) measurement was carried out to explore the changes in functional groups of Ag/ZnO by Nicolet IS50. UV-Vis diffuse reflectance spectra of the as-synthesized samples were measured on a UV-Vis-NIR spectrometer (Cary 500).

2.5. Photocatalytic Experiment. The photodegradation of BPA was performed in a Pyrex beaker using the as-synthesized sample as a photocatalyst under visible light (250 W Hg lamp). BPA (20 mg/L) solution was prepared in 100 mL distilled water and mixed with 50 mg of catalyst. The mixture was stirred at a constant rate of 200 rpm. At regular time intervals for 30 min, analysis samples were taken from the reaction suspension and then filtered by a syringe filter (0.45 μm PTFE membrane) to remove the catalyst. The BPA concentration of the filtrate was analyzed by a UV-Vis spectrophotometer (Agilent 8453) at the maximum absorbance wavelength of 277 nm. The degradation efficiency and degradation capacity of BPA were calculated by the following equations:

$$\text{Degradation efficiency}\,(\%) = \frac{C_{0-}C_t}{C_0} \times 100, \tag{1}$$

$$\text{Degradation capacity}\left(\frac{\text{mg}}{\text{g}}\right) = \frac{(C_{0-}C_t) \times V}{m}. \tag{2}$$

The degradation rate of BPA was determined by fitting the degradation profile with the first-order kinetic model, as presented by the following equation:

$$\ln \frac{C_0}{C_t} = k_{ap} \times t, \tag{3}$$

where k_{ap} (min^{-1}) is the rate constant, C_0 is the initial concentration of dye, C_t is the concentration of BPA in time (mg/L), V is the volume of BPA solution (L), m is the mass of the catalyst (g), and t is the reaction time (min).

3. Results and Discussion

3.1. Characterization of the Catalyst. Figure 1 shows the SEM, EDS, and TEM images of the ZnO and Ag/ZnO-10 nanocomposite. ZnO showed an aggregated morphology (Figure 1(a)) consisting of many small particles with approximately 20 nm in size (Figure 1(b)). When Ag was doped into the composite, the morphology of Ag/ZnO-10 at low magnification (Figure 1(c)) was like ZnO, but at the higher magnification, it showed more aggregate than ZnO, and the Ag/ZnO sheets were observed in Figure 1(d). The elemental maps for Ag and Zn shown in Figures 1(e) and 1(f) indicated a good dispersion of Ag in the composite; nanoparticles were observed with high dispersion in the EDS layered image (Figure 1(g)). The EDS spectrum in Figure 1(h) showed the Ag, Zn, and O elements at the contents of 8.0, 68.0, and 15.8%, respectively. The TEM images (Figures 1(i) and 1(j)) and HR-TEM image (Figure 1(k)) gave the additional evidence of the dispersion of Ag in composite; Ag was crystal particles with the particle size of about 10-20 nm in Figures 1(i)–1(k). This result was consistent with the obtained results from SEM and element mapping.

Figure 2 shows the XRD patterns of the ZnO and Ag/ZnO-10 nanocomposite. The diffraction peaks corresponding to (100), (002), (101), (102), (110), (103), (112), (201), and (202) planes were observed for pure ZnO; these could be indexed hexagonal wurtzite structure of ZnO (JCPDS 36–1451) [3]. These peaks were also seen in the Ag/ZnO-10 composite. The diffraction peaks corresponding to (111) and (200) of Ag were observed at 38.2 and 44.7°, respectively (JCPDS 04–0783) [43–45]. Moreover, there were no characteristic peaks of impurity phases such as Zn, $Zn(OH)_2$, and $Zn(OH)_2CO_3$ which were observed indicating the high purity of ZnO and Ag/ZnO-10 samples.

To study the effect of silver doping on the average crystallite size, the mean crystal size was estimated from the Debye–Scherrer equation as follows:

$$D = \frac{K\lambda}{\beta \cos\theta}, \tag{4}$$

where K is a dimension shape factor, a typical value of about 0.9, but varies with the actual shape of the crystallite; λ is the wavelength of X-ray used (1.5406 Å), β is the full width at half maximum intensity (FWHM) in radians, and θ is Bragg's diffraction angle. In order to obtain more detailed structural analyses, the Rietveld refinement method was applied to XRD data. The Rietveld refinement analyses were carried out using the FullProf program. The analytical results are shown in Table 1.

The change in the lattice parameters (a and c) from 3.251 ± 0.005 Å and 5.212 ± 0.002 Å for pure ZnO to 3.253 ± 0.007 Å and 5.215 ± 0.003 Å for Ag/ZnO-10 sample is observed; it clearly indicated the increase in the lattice size upon doping of Ag leading to the increase of the unit cell volume from 47.704 Å^3 for ZnO to 47.790 Å^3 for Ag/ZnO-10 because the radius of Ag^+ (114 pm) is larger than Zn^{2+} (74 pm) and substitution of Ag^+ ions in the lattice is larger

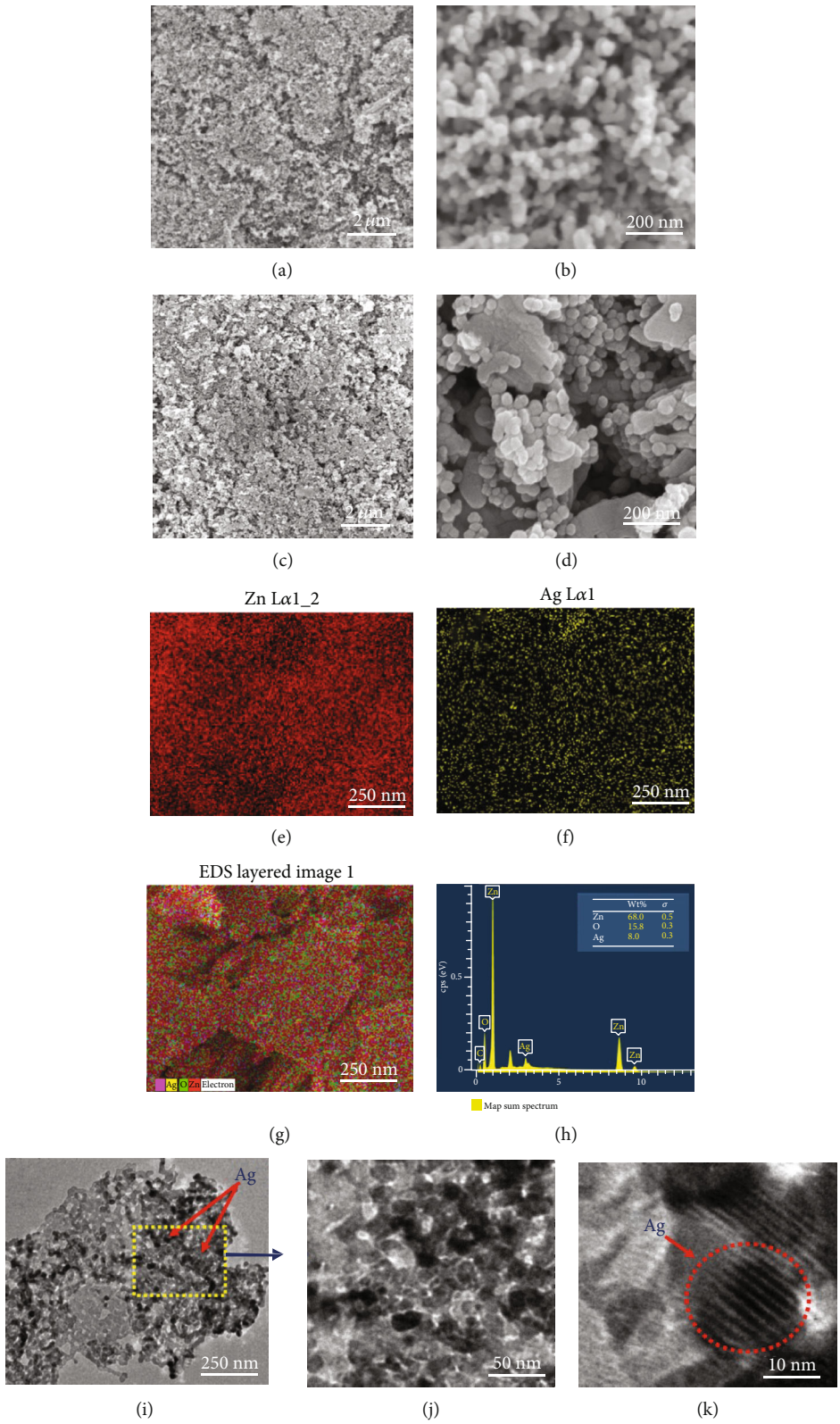

Figure 1: (a, b) SEM images of nano ZnO with the different scale bars; (c, d) SEM images with the different scale bars of the Ag/ZnO-10 nanocomposite; (e, f) element mapping images of Zn and Ag, respectively; (g, h) EDS layered image and EDS spectrum, respectively; (i, j) TEM images with the different scale bars; (k) HR-TEM image of the Ag/ZnO-10 nanocomposite.

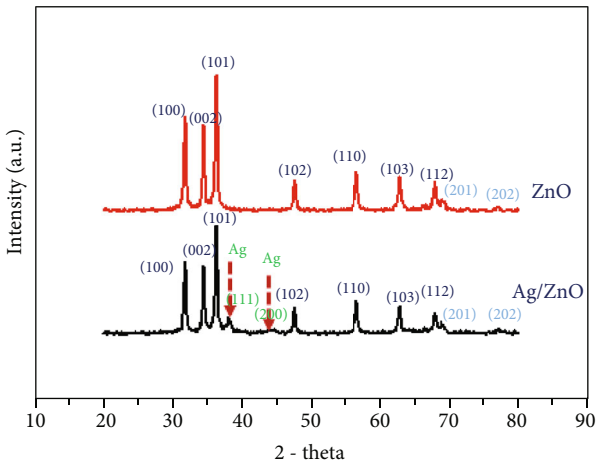

FIGURE 2: XRD patterns of ZnO and Ag/ZnO-10 nanocomposite.

than Zn^{2+} ions [46, 47]. The crystalline sizes of ZnO and Ag/ZnO-10 samples were estimated as 20.1 and 19.6 nm, respectively. These are consistent with the obtained results from SEM and TEM in Figure 1.

Figure 3 presents the N_2 adsorption/desorption isotherms and pore size distributions of the ZnO and Ag/ZnO-10 nanocomposite. According to the IUPAC classification, N_2 adsorption/desorption isotherms were type IV with H_3 hysteresis loop (Figure 3(a)), but the hysteresis loop of Ag/ZnO-10 was much lower than that of pure ZnO. Moreover, the hysteresis loops of both samples approached $P/P_o = 1$, indicating the presence of mesoporous and macropore together in both samples. Figure 3(b) shows the pore with distributions, which was determined by the Barrett-Joyner-Halenda (BJH) method from the desorption branch of the isotherm. Both samples showed a mixture of pore size, but it could be seen that most of the pore possessed width in the range of 5-50 nm. The BET surface area, pore volume, and BJH average pore size were of composite slightly decreased with the doping of silver. BET surface areas were 26.2 and 24.2 m^2/g, pore volumes were 0.48 and 0.21 cm^3/g, and BJH average pore sizes were 26.8 and 21.1 cm^3/g for ZnO and Ag/ZnO-10, respectively. Although samples were prepared by facile precipitation method, the surface areas of ZnO nanoparticles and Ag/ZnO nanocomposite were relatively high as compared to other samples in previous publications [48, 49]. In comparison, the pore size distributions of samples were analyzed by density functional theory (DFT) method. The DFT average pore size of ZnO was larger than that of Ag/ZnO, but the average pore size from the DFT method was larger than that of the BJH method as seen in Table 2.

Figure 4 presents the FTIR spectra of the ZnO and Ag/ZnO-10 nanocomposite. The broad band at 3429 cm^{-1} in ZnO could be assigned to the O–H stretching vibration of water. This peak became weaker and shifts to lower wavenumber at 3406 cm^{-1} indicating that the addition of silver into composite led to decreased absorption of water on the surface of the sample. The peaks at 1636, 1509, and 1404 cm^{-1} corresponded to the C=O stretching modes and O=C=O bonds due to the adsorption of CO_2 on the surface of the ZnO and Ag/ZnO nanocomposite. The peak location at 470 cm^{-1} was assigned to the vibration of Zn–O in the lattice of the hexagonal wurtzite phase of ZnO.

Figure 5 shows the UV-Vis diffuse reflectance spectra and Tauc's plot of ZnO and Ag/ZnO composites. The adsorption of Ag/ZnO composites was shifted to the longer wavelength from ZnO with the increase of the molar ratio of Ag/ZnO. The adsorption edges of Ag/ZnO-2 and Ag/ZnO-5 composites were steeper than those of ZnO, but it was similar to Ag/ZnO-10. When the molar ratio of Ag/ZnO increased to 15, the adsorption of the composite was shifted to a shorter wavelength from Ag/ZnO-10, showing a similarity to the shape of Ag/ZnO-5 (Figure 5(a)). The $h\nu$ values were plotted against $(\alpha h\nu)^2$ and extended to calculate the band gap energy of as-synthesized samples by Tauc's method [50]; the results are presented in Figure 5(b). The band gap energy of ZnO was 3.220 eV. This was lower than that of Ag/ZnO-2 composite (3.230 eV) but larger than that of other composites; the band gap energies were 3.205, 3.125, and 3.181 eV for Ag/ZnO-5, Ag/ZnO-10, and Ag/ZnO-15, respectively. These results indicated that the doping of Ag into composite at the higher molar ratio than 2 reduced the band gap energy; it could increase the photocatalytic activity of composite under visible light.

3.2. Photodegradation of BPA

3.2.1. Effect of Ag Doping on Photodegradation of BPA. Figure 6 presents the effect of silver doping on photocatalytic degradation of BPA under visible light irradiation. The degradation efficiency in 120 min and reaction rate of BPA in pure ZnO were 32.7% and 0.003 min^{-1}, respectively. The degradation efficiency of BPA increased when silver doped in the composite. The degradation efficiency and reaction rate increased to 49.9% and 0.005 min^{-1}, respectively, although the band gap energy of Ag/ZnO-2 composite was larger than that of ZnO. At the higher molar of Ag/ZnO than 2, the degradation efficiency and reaction rate increased when the molar ratio increased; the degradation efficiencies were 79.9 to 100% and the reaction rates were 0.008 to 0.014 min^{-1} for Ag/ZnO-5 and Ag/ZnO-10 composites, respectively. With a further increase in the molar ratio of Ag/ZnO, the degradation efficiency was decreased.

The photocatalytic mechanism of BPA on Ag/ZnO composite under visible light irradiation is presented in Figure 7. When visible light was irradiated to the surface of ZnO, the photons can excite electrons in the valence band (VB) to be moved up to the conduct band (CB); the electron and hole pair (e^- and h^+) is generated. They can interact with water and oxygen on the surface of ZnO to generate oxidizing agents including H_2O_2, $^{\cdot}O_2^-$, and $^{\cdot}OH$, in which $^{\cdot}O_2^-$ and $^{\cdot}OH$ are the strong oxidizing agents; they can decompose the organic compound into CO_2 and H_2O_2. However, the time of electrons (e^-) lying on the conduction band is extremely short; the electron (e^-) almost intermediately releases the energy to return to the ground state to recombine with hole (h^+) originally. This is the significant limitation of pure ZnO nanoparticles.

Table 1: Lattice parameters and crystallite sizes of ZnO and Ag/ZnO-10.

Sample	Crystal system	Space group	Crystallite size (nm)	Lattice parameter, a (Å)	Lattice parameter, c (Å)	Cell volume (Å^3)
ZnO	Hexagonal	P63 mc	20.1	3.251 ± 0.005	5.212 ± 0.002	47.704
Ag/ZnO-10	Hexagonal	P63 mc	19.6	3.253 ± 0.007	5.215 ± 0.003	47.790

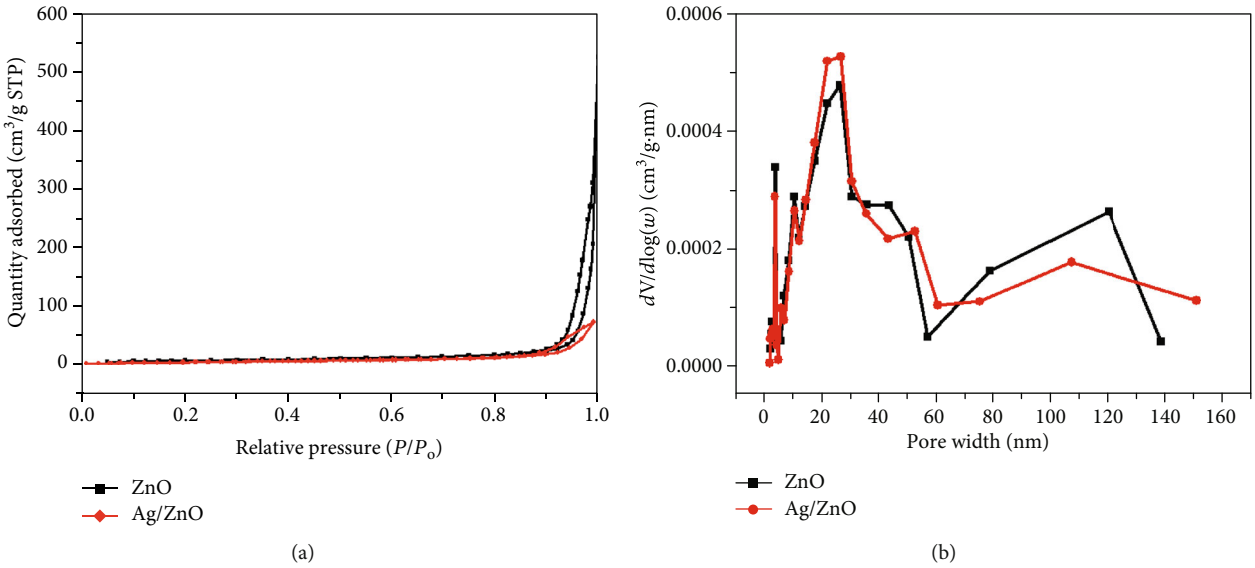

Figure 3: (a) N_2 adsorption/desorption isotherms and (b) pore size distributions of ZnO and Ag/ZnO-10 nanocomposite.

Table 2: The textural properties of ZnO and Ag/ZnO-10 composite.

Samples	S_{BET} (m^2/g)	BJH pore volume (cm^3/g)	BJH average pore size (nm)	DFT average pore size (nm)
ZnO	26.2	0.48	26.9	30.1
Ag/ZnO-10	24.2	0.21	21.1	25.2

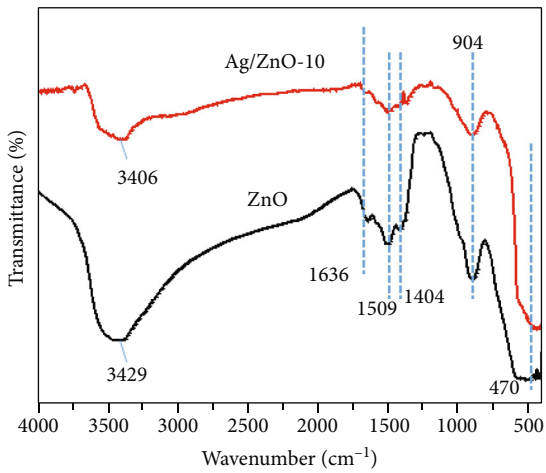

Figure 4: FTIR spectra of the ZnO and Ag/ZnO-10 nanocomposite.

In the presence of Ag metal, the Schottky barrier is formed between Ag and ZnO due to the energy level of CB of ZnO which is higher than the Fermi level of Ag/ZnO leading to free electrons in CB that can transfer from ZnO to Ag as described by the red arrow shown in Figure 7(b), thereby preventing the recombination between electrons and holes on the surface of ZnO. The electron on Ag nanoparticles can produce the $^{\cdot}O_2^-$ free radical, while the holes in the VB can react with H_2O_2 to produce $^{\cdot}OH$ radical. These free radicals can degrade organic compounds to CO_2 and H_2O. These can be explained by the following equations:

$$ZnO + h\nu \rightarrow ZnO(e^-) + h^+ \quad (5)$$

$$ZnO\,(e^-) + Ag \rightarrow ZnO + Ag\,(e^-) \quad (6)$$

$$Ag\,(e^-) + O_2 \rightarrow {}^{\cdot}O_2^- + Ag \quad (7)$$

$$ZnO\,(h^+) + H_2O \rightarrow ZnO + H^+ + {}^{\cdot}OH \quad (8)$$

$$({}^{\cdot}O_2^- + {}^{\cdot}OH) + BPA \rightarrow \text{Intermediate products} \quad (9)$$

$$({}^{\cdot}O_2^- + {}^{\cdot}OH) + \text{Intermediate products} \rightarrow CO_2 + H_2O \quad (10)$$

On the other hand, under visible light irradiation, the pure ZnO exhibited weak photocatalytic activity for degradation of BPA due to the fact that ZnO absorbs weakly in the visible light region, while the Ag/ZnO composites showed significantly enhanced photocatalytic activity, because under visible light irradiation electrons can be formed in the

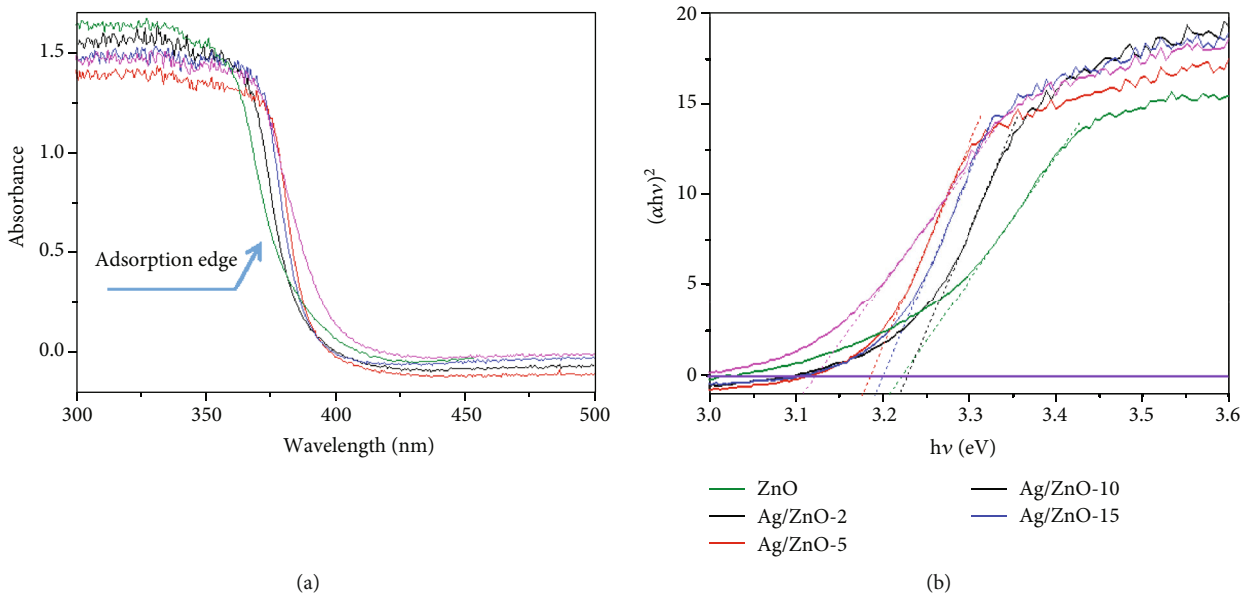

Figure 5: (a) UV-Vis diffuse reflectance spectra and (b) Tauc's plot of the as-synthesized samples.

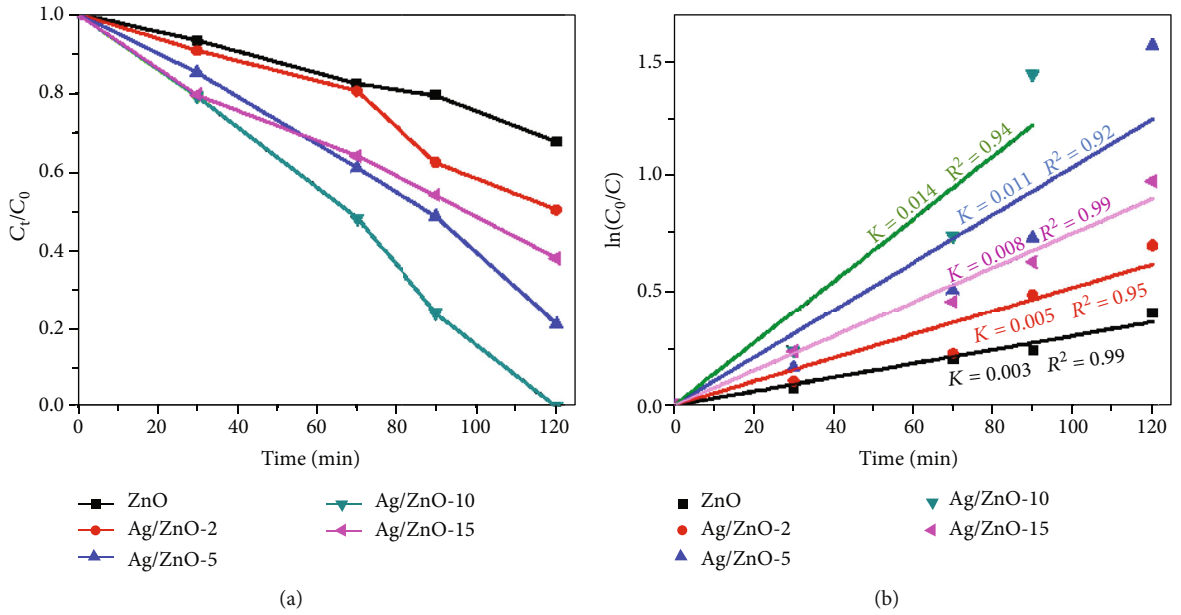

Figure 6: (a) Photodegradation of BPA in ZnO and Ag/ZnO and (b) the kinetic curves (the reaction conditions: dosage catalyst 0.5 g/L, BPA concentration of 20 mg/L, and pH = 6.0).

metallic Ag nanoparticles through the strong SPR effect, leading to strong absorption light in the visible region. Nevertheless, the Schottky barrier formed at the metal-semiconductor interface can hinder the transfer of electrons from Ag nanoparticles to ZnO. Up to now, many studies have proven that electrons can overcome the Schottky barrier at the interface because of its strong electron oscillating collectively on the SPR excitation [51–53]. Therefore, electrons can transfer from Ag to the CB of ZnO as illustrated by the green arrow in Figure 7(b). Then, they are scavenged by adsorbed oxygen molecules to yield superoxide radical anions ($^{\cdot}O_2^-$) to degrade BPA molecules. Meanwhile, the photogenerated holes could transfer to the photocatalyst surface and directly oxidize the organic pollutants, resulting in an improved photocatalytic activity in the visible light region.

3.2.2. Effect of Catalyst Dosage on the Degradation of BPA. To investigate the influence of a catalyst mount, the catalytic oxidation experiments were carried out by employing the Ag/ZnO-10 composite at the different dosages (0.025, 0.050, 0.075, and 0.100 g) under constant reaction conditions: BPA concentration of 20 mg/L and pH = 6.0. The

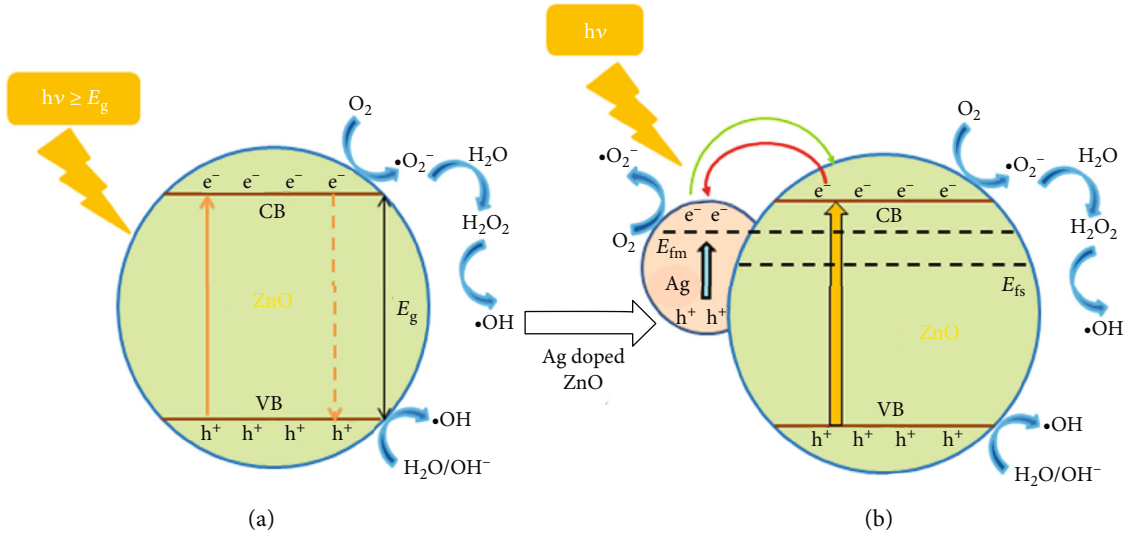

Figure 7: Photocatalytic mechanism of BPA in Ag/ZnO nanocomposite under visible light.

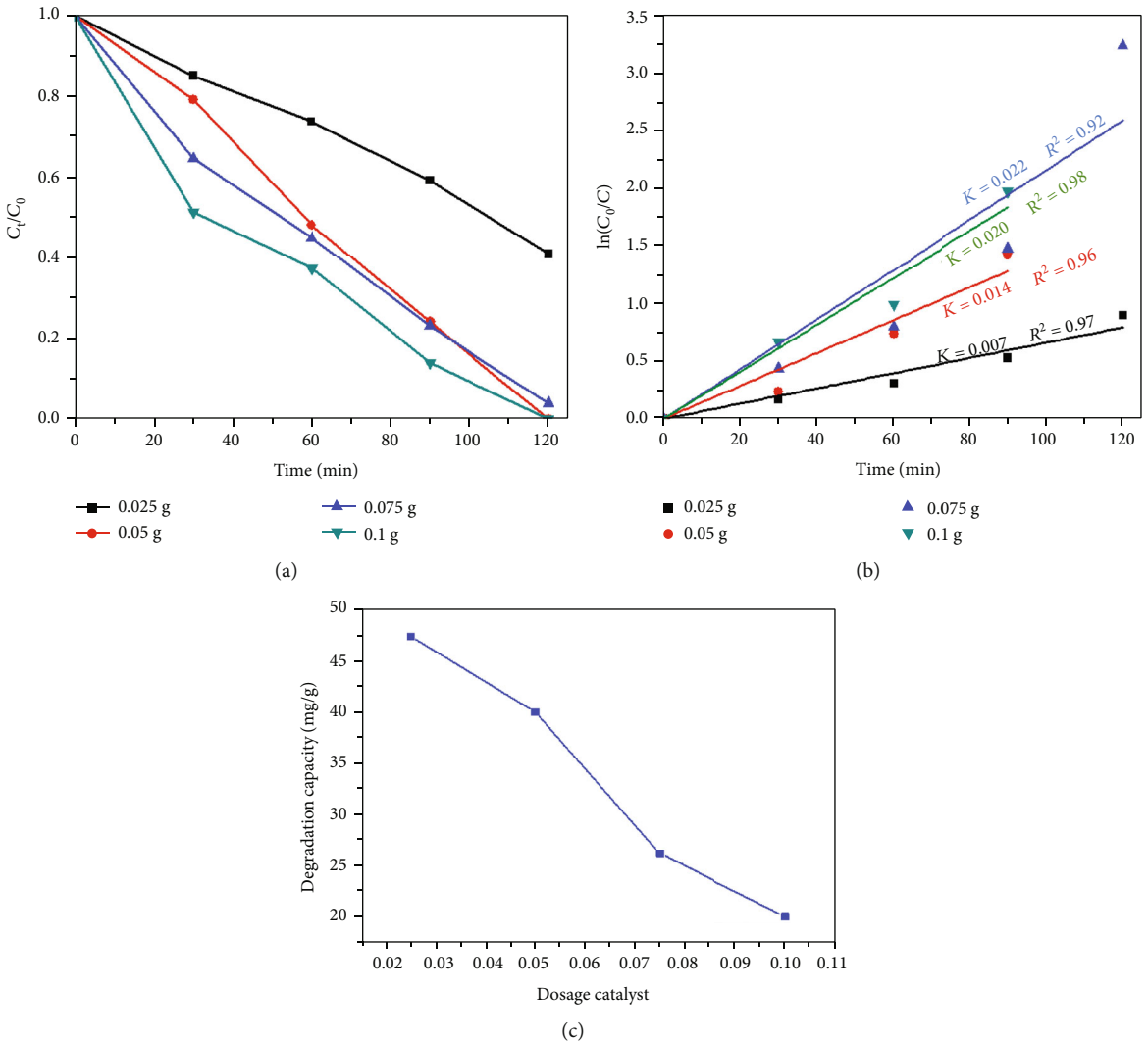

Figure 8: (a) Effect of dosage catalyst on photodegradation of BPA, (b) the kinetic curves, and (c) degradation capacity versus dosage catalyst. The reaction conditions are as follows: BPA concentration of 20 mg/L and pH = 6.0.

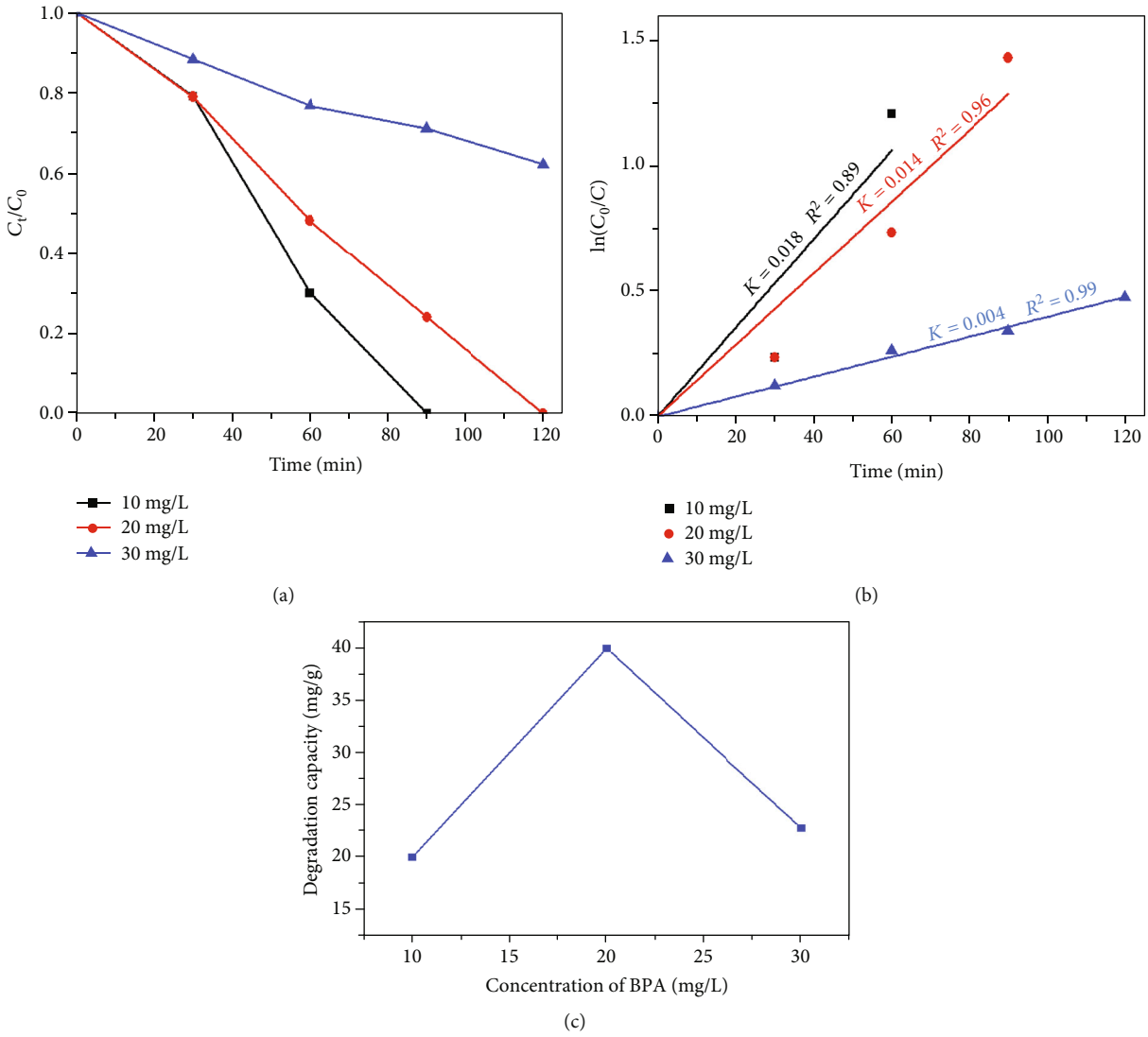

FIGURE 9: (a) Effect of concentration of BPA on photocatalytic activity, (b) the kinetic curves, and (c) degradation capacity versus concentration of BPA. The reaction conditions are as follows: dosage catalyst of 0.05 g and pH = 6.0.

catalytic efficiency as a function of catalyst amount is showed in Figure 8. It could be seen that the degradation efficiency and reaction rate of BPA increased with an increase in the dosage catalyst. The degradation efficiencies were 9.24, 100, 96.08, and 100% and reaction rates were 0.007, 0.014, 0.020, and 0.022 min^{-1} at the catalyst dosage of 0.025, 0.050, 0.075, and 0.100 g, respectively. And the correlation coefficient (R^2) values were in the range of 0.92-0.98 (Figure 8(b)). However, the degradation capacity decreased from 47.4 to 20 mg/g when the dosage catalyst increased from 0.025 to 0.100 g (Figure 8(c)).

Since the increase of catalyst dosage leads to an increase in the number of active sites on the surface of catalysts, the density of catalyst particles in the area of illumination is improved [54]. However, the degradation capacity of BPA per gram of catalyst was decreased with an increase in the catalyst dosage, as shown in Figure 8(c), due to increasing the suspended catalysts in a solution. The short wave tail photons are not able to enter the reaction mixture and a decrease in visible light penetration increasing in scattering effect [55, 56]. Also, as more catalyst was added, each catalyst has less chance to contact with BPA molecules because of fast reaction as shown in Figure 8(a). As a result, the reaction performance and rate can be improved with increasing catalyst dosage, but degradation capacity became smaller.

3.2.3. Effect of BPA Concentration on Photodegradation. The effect of the concentration of BPA on the photocatalytic activity of the catalyst is presented in Figure 9. The degradation efficiency and reaction rate were decreased with the concentration of BPA. The degradation efficiency was achieved 100% in 90 min for the concentration of 10 mg/L, showing the reaction rate of 0.018 min^{-1}. The degradation efficiency at 20 mg/L was also 100%, but at a lower reaction rate of 0.014 min^{-1}. The degradation

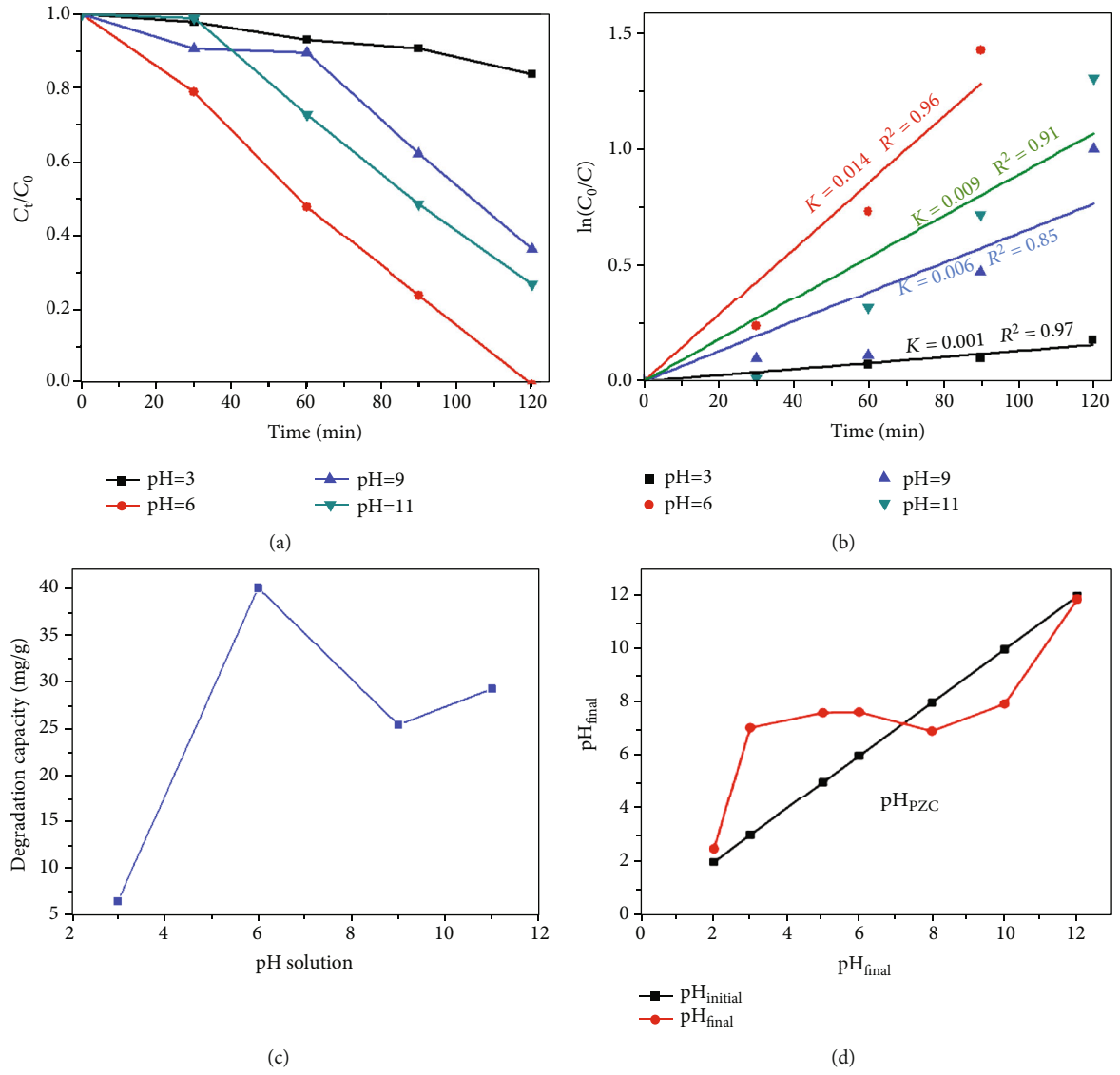

FIGURE 10: (a) Effect of pH solution on the degradation of BPA, (b) the kinetic curves, (c) degradation capacity versus pH solution, and (d) the pH_{PZC} determination of Ag/ZnO. The reaction conditions are as follows: dosage catalyst of 0.05 g and BPA concentration of 20 mg/L.

efficiency and reaction rate were 38.1% and 0.004 min^{-1} at a high concentration of 30 mg/L, respectively. R^2 values were in the range of 0.89-0.99.

The negative effect of increased amount of BPA on reaction can be interpreted by the following reasons. (1) The number of BPA molecules, adsorbed on the active sites of the catalyst surface, increases with the initial concentration of BPA. Therefore, the generation rate of $O_2^{\cdot-}$ and $OH^{\cdot}$ radicals on the same active sites became decreased. (2) Alternatively, increasing the dye concentration leads to generating many intermediates form dye molecules along with the reaction and may compete with BPA molecules in the constant total active sites. Despite lowering the degradation efficiency and reaction rate of BPA with increasing the initial concentration of BPA, the degradation capacity at 20 mg/L of 40 mg/g was higher than that of other concentrations (Figure 9(c)).

3.2.4. Effect of Solution pH. The pH value of wastewater is an important factor for well-designed reaction processes. It has a great influence not only on the functional groups and surface charges of adsorbents but also on the structure and ionization degree of pollutant molecules [57]. In this study, the effect of initial solution pH on the degradation of BPA by the as-synthesized Ag/ZnO-10 composite was investigated. The performance was evaluated at a wide range of pH values from 3.0 to 11.0 under the fixed other conditions (dosage catalyst of 0.05 g and BPA concentration of 20 mg/L).

Figure 10 presents the degradation of BPA with time at different values. The pH gave a critical impact on the degradation performance of BPA. When pH increased from 3.0 to 6.0, the degradation efficiency significantly increased from 16.3 to 100%, showing an improved reaction rate from 0.001 to 0.014 min^{-1} and enhanced degradation capacity from 6.25 to 40 mg/g (Figures 10(b) and 10(c)). At pH value

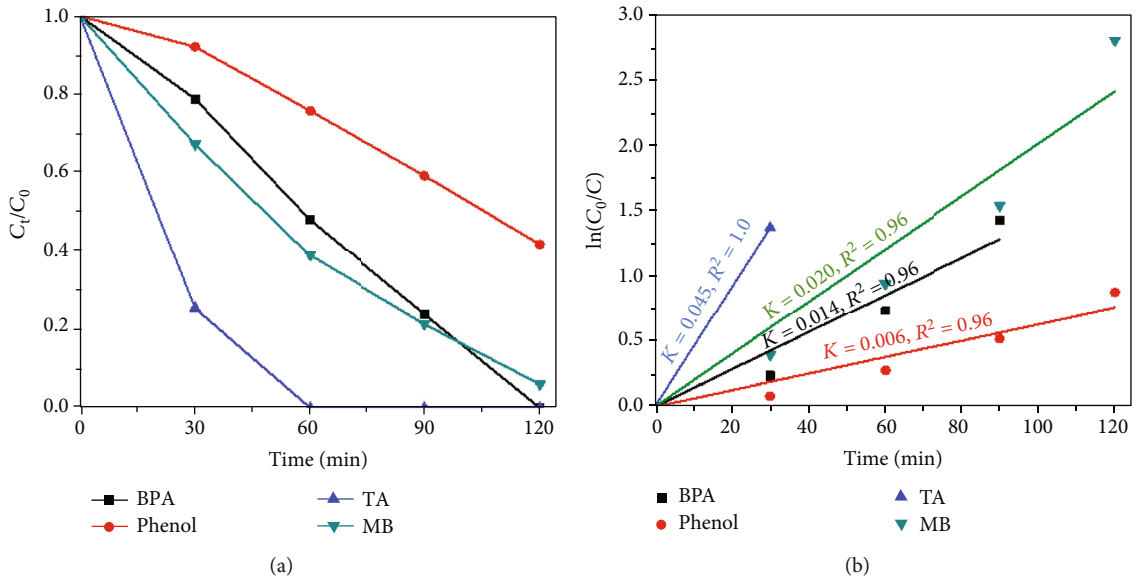

Figure 11: Degradation of the different persistent organic compounds in Ag/ZnO-10 composite. The reaction conditions are as follows: dosage catalyst of 0.05 g, BPA concentration of 20 mg/L, and pH = 6.0.

Table 3: Comparison of photocatalytic degradation of BPA by various catalysts.

Catalyst	Reaction conditions	Observation	Reference
6.3% $H_3PW_{12}O_{40}/TiO_2$ composite film	$[BPA] = 5\ mg/L$, $pH = 8.2$, under light irradiation of Xenon lamp 300 W	100% of BPA was removed in 240 min.	[58]
2% Ce-ZnO	$[Cat.] = 1\ g/L$, $[BPA] = 50\ mg/L$, $pH = 7.3$, $[H_2O_2] = 5.10^{-3}\ M$, under UV light irradiation	67% of BPA was removed in 180 min.	[59]
GO@BiOI/Bi_2WO_6	$[Cat.] = 0.5\ g/L$, $[BPA] = 10\ mg/L$, $pH = 7$, under Xenon illumination (500 W)	81% of BPA was removed in 5 h.	[30]
4% C–ZnO	$[Cat.] = 1\ g/L$, $[BPA] = 50\ mg/L$, $pH = 8$, $[H_2O_2] = 5.10^{-3}\ M$, under UV lamp 30 W	100% of BPA was removed in 24 h.	[60]
1.5% Pd/mpg-C_3N_4 composite	$[Cat.] = 0.5\ g/L$, $[BPA] = 20\ mg/L$, under Xenon 350 W, in a wide range of pH (3.1-11.0)	Almost 100% of BPA was removed in 360 min.	[61]
ZnO nanoparticles	$[Cat.] = 0.5\ g/L$, $[BPA] = 20\ mg/L$, $pH = 6.0$, under visible light irradiation	32.7% of BPA was removed in 120 min, degradation capacity of 13.08 mg/g.	This work
Ag/ZnO-10 composite	$[Cat.] = 0.5\ g/L$, $[BPA] = 20\ mg/L$, $pH = 6.0$, under visible light irradiation	100% of BPA was removed in 120 min, degradation capacity of 40 mg/g.	This work

higher than 6.0, the reaction performance was decreased, the degradation efficiencies were 63.4 and 73%, and the reaction rates were 0.006 and 0.009 min^{-1} at pH = 9.0 and 11.0, respectively. And R^2 values were in the range of 0.85-0.97.

It was observed that the optimum pH for efficient degradation of BPA on Ag/ZnO-10 composite is 6.0. At lower pH than 6.0, the degradation efficiency is low; it is due to the dissolution of ZnO in an acid medium (equation (11)). At higher pH than 6, the efficient degradation is also low due to the dissolution of ZnO in an alkaline medium (equation (12)).

$$ZnO(s) + 2H^+(aq) \rightarrow Zn^{2+} + H_2O \quad (11)$$

$$ZnO(s) + 2OH^-(aq) \rightarrow ZnO_2^- + H_2O \quad (12)$$

On the other hand, the surface charge property of nanoparticles, which depends on the pH point of zero charge (pH_{PZC}), is also the reason affecting the adsorption properties of dye molecules on the surface of photocatalyst. The pH_{PZC} of Ag/ZnO measured by the pH drift method reached 7.4, as shown in Figure 10(d). Hence, at the pH of 6.0, the catalytic surface will adsorb efficiently the organic anion (BPA donated protons) and lead to enhanced significant degradation of BPA on the Ag/ZnO composite.

3.2.5. Degradation of Other Organic Compounds and Comparison of Degradation of BPA with Other Catalysts. The degradation efficiency of organic compounds by photocatalysts depends not on only catalyst properties, such as surface area, pore volume and pore size distribution, and

composition, but also on the characteristics of organic compounds. Therefore, the optimum condition for the degradation of the certain organic compounds depends on the characteristics of catalysts and solutions. In this study, the photocatalytic performance of Ag/ZnO-10 composite was evaluated by other persistent organic compounds such as phenol, tartrazine (TA), and methylene blue (MB) at the reaction conditions as follows: dosage catalyst of 0.05 g, BPA concentration of 20 mg, and pH of 6.0. As shown in Figure 11, the reaction efficiency and reaction rate ascended gradually from phenol to BPA, MB, and TA. The Ag/ZnO-10 composite showed a highly photocatalytic degradation of TA, showing the degradation efficiency and reaction rate of 100% in 60 min and 0.045 min^{-1}.

Table 3 shows a brief comparison of BPA removal efficiency by different catalysts through photocatalytic activity. It could be observed that the degradation efficiency and reaction rate of the Ag/ZnO-10 composite under visible light irradiation were much higher than those of ZnO when adding C or Ce under UV light irradiation. In comparison with other catalysts such as $H_3PW_{12}O_{40}/TiO_2$, GO@BiOI/-Bi_2WO_6, and Pd/mpg-C_3N_4, which remove BPA under simulated solar light irradiation by Xenon lamp, the degradation rate of BPA on Ag/ZnO-10 was also faster. Therefore, the Ag/ZnO-10 composite is expected as a good and eco-friendly catalyst in the removal of BPA from wastewater.

4. Conclusion

ZnO nanoparticles and Ag/ZnO nanocomposite were successfully prepared by the facile method. ZnO nanoparticles were approximately 20 nm in size and could degrade BPA under visible light irradiation showing the degradation efficiency and the reaction rate of 32.7% and 0.003 min^{-1}, respectively. When Ag was doped into composites at the molar ratio of Ag/ZnO larger than 2, the band gap energy of composite was decreased, and the degradation efficiency and the reaction rate increase. In comparison with the surface area and pore volume of the composite, the increase in degradation efficiency of BPA in composite mainly depended on the rate of electrons transferring from VB to CB and the recombination of electrons, in which the band gap energy and Ag content played a decisive role. At the Ag/ZnO ratio of 10, the composite approached the highest photocatalytic performance showing the degradation efficiency, reaction rate, and degradation capacity of 100%, 0.014 min^{-1}, and 40 mg/g, respectively. The optimal reaction conditions for the removal of BPA under visible light irradiation of Ag/ZnO-10 were pH of 6.0, catalyst dosage of 0.1 g, and BPA concentration of 10 mg/L for considering of degradation efficiency, which were pH = 6.0, catalyst dosage of 0.025 g, and BPA concentration of 20 mg/g for considering the degradation capacity. Moreover, the catalytic performance of Ag/ZnO-10 composite was tested by degrading other persistent organic compounds. The reaction efficiency and the reaction rate increased gradually from phenol to BPA, MB, and TA, showing the degradation efficiency and reaction rate of 100% in 60 min and 0.045 min^{-1} for TA. These results indicated the highly potential application of composite in the removal of toxic organic compounds in wastewater.

Data Availability

The research data used to support the findings of this study are included within the article.

Conflicts of Interest

The authors declare that there is no conflict of interest.

Acknowledgments

The authors are grateful for the financial support of Vietnam National Foundation for Science and Technology Development (NAFOSTED) under grant number 104.05-2018.333.

References

[1] E. Mohagheghpour, F. Moztarzadeh, M. Rabiee et al., "Micro-Emulsion Synthesis, Surface Modification, and Photophysical Properties of Zn_{1-x} Mn_x S Nanocrystals for Biomolecular Recognitio," *IEEE Transactions on Nanobioscience*, vol. 11, no. 4, pp. 317–323, 2012.

[2] C. B. Ong, L. Y. Ng, and A. W. Mohammad, "A review of ZnO nanoparticles as solar photocatalysts: synthesis, mechanisms and applications," *Renewable and Sustainable Energy Reviews*, vol. 81, pp. 536–551, 2018.

[3] V. A. Tu and V. A. Tuan, "A facile and fast solution chemistry synthesis of porous ZnO nanoparticles for high efficiency photodegradation of tartrazine," *Vietnam Journal of Chemistry*, vol. 56, no. 2, pp. 214–219, 2018.

[4] R. Suntako, "Effect of synthesized ZnO nanograins using a precipitation method for the enhanced cushion rubber properties," *Materials Letters*, vol. 158, pp. 399–402, 2015.

[5] P. Pascariu and M. Homocianu, "ZnO-based ceramic nanofibers: preparation, properties and applications," *Ceramics International*, vol. 45, no. 9, pp. 11158–11173, 2019.

[6] X. Yang, C. Zhang, A. Li, J. Wang, and X. Cai, "Red fluorescent ZnO nanoparticle grafted with polyglycerol and conjugated RGD peptide as drug delivery vehicles for efficient target cancer therapy," *Materials Science and Engineering: C*, vol. 95, pp. 104–113, 2019.

[7] C. García-Gómez, S. García-Gutiérrez, A. Obrador, and M. D. Fernández, "Study of Zn availability, uptake, and effects on earthworms of zinc oxide nanoparticle *versus* bulk applied to two agricultural soils: acidic and calcareous," *Chemosphere*, vol. 239, article 124814, 2020.

[8] M. Baudys, J. Krýsa, M. Zlámal, and A. Mills, "Weathering tests of photocatalytic facade paints containing ZnO and TiO_2," *Chemical Engineering Journal*, vol. 261, pp. 83–87, 2015.

[9] M. A. Bhatti, A. A. Shah, K. F. Almani et al., "Efficient photo catalysts based on silver doped ZnO nanorods for the photo degradation of methyl orange," *Ceramics International*, vol. 45, no. 17, pp. 23289–23297, 2019.

[10] V. Sogne, F. Meier, T. Klein, and C. Contado, "Investigation of zinc oxide particles in cosmetic products by means of centrifugal and asymmetrical flow field-flow fractionation," *Journal of Chromatography A*, vol. 1515, pp. 196–208, 2017.

[11] P. Sánchez-Cid, C. Jaramillo-Páez, J. A. Navío, A. N. Martín-Gómez, and M. C. Hidalgo, "Coupling of Ag_2CO_3 to an optimized ZnO photocatalyst: advantages *vs.* disadvantages," *Journal of Photochemistry and Photobiology A: Chemistry*, vol. 369, pp. 119–132, 2019.

[12] M. R. D. Khaki, M. S. Shafeeyan, A. A. A. Raman, and W. M. A. W. Daud, "Application of doped photocatalysts for organic pollutant degradation - a review," *Journal of Environmental Management*, vol. 198, Part 2, pp. 78–94, 2017.

[13] N. Yu, H. Peng, L. Qiu et al., "New pectin-induced green fabrication of Ag@AgCl/ZnO nanocomposites for visible-light triggered antibacterial activity," *International Journal of Biological Macromolecules*, vol. 141, pp. 207–217, 2019.

[14] A. Stanković, S. Dimitrijević, and D. Uskoković, "Influence of size scale and morphology on antibacterial properties of ZnO powders hydrothemally synthesized using different surface stabilizing agents," *Colloids and Surfaces B: Biointerfaces*, vol. 102, pp. 21–28, 2013.

[15] N. Neves, A. Lagoa, J. Calado et al., "Al-doped ZnO nanostructured powders by emulsion detonation synthesis – Improving materials for high quality sputtering targets manufacturing," *Journal of the European Ceramic Society*, vol. 34, no. 10, pp. 2325–2338, 2014.

[16] B. P. Zhang, N. T. Binh, K. Wakatsuki et al., "Pressure-dependent ZnO nanocrsytal growth in a chemical vapor deposition process," *The Journal of Physical Chemistry B*, vol. 108, no. 30, pp. 10899–10902, 2004.

[17] M. Park, S.-H. Lee, D. Kim, J. Kang, J.-Y. Lee, and S. M. Han, "Fabrication of a combustion-reacted high-performance ZnO electron transport layer with silver nanowire electrodes for organic solar cells," *ACS Applied Materials & Interfaces*, vol. 10, no. 8, pp. 7214–7222, 2018.

[18] H. V. Vasei, S. M. Masoudpanah, M. Adeli, and M. R. Aboutalebi, "Solution combustion synthesis of ZnO powders using CTAB as fuel," *Ceramics International*, vol. 44, no. 7, pp. 7741–7745, 2018.

[19] Y. Hu, Q. Zhu, X. Yan, C. Liao, and G. Jiang, "Occurrence, fate and risk assessment of BPA and its substituents in wastewater treatment plant: a review," *Environmental Research*, vol. 178, article 108732, 2019.

[20] M. Clinic, "Nutrition and Healthy Eating," in *Healthy Lifestyle*, B. A. Bauer, Ed., Mayo Clinic, 2019.

[21] K. V. A. Kumar, B. Lakshminarayana, T. Vinodkumar, and C. Subrahmanyam, "Cu-ZnO for visible light induced mineralization of Bisphenol-A: impact of Cu ion doping," *Journal of Environmental Chemical Engineering*, vol. 7, no. 3, article 103057, 2019.

[22] H. C. Alexander, D. C. Dill, L. W. Smith, P. D. Guiney, and P. Dorn, "Bisphenol a: acute aquatic toxicity," *Environmental Toxicology and Chemistry*, vol. 7, no. 1, pp. 19–26, 1988.

[23] K. Pelch, J. A. Wignall, A. E. Goldstone et al., "A scoping review of the health and toxicological activity of bisphenol A (BPA) structural analogues and functional alternatives," *Toxicology*, vol. 424, article 152235, 2019.

[24] M. F. Brugnera, K. Rajeshwar, J. C. Cardoso, and M. V. B. Zanoni, "Bisphenol A removal from wastewater using self-organized TIO_2 nanotubular array electrodes," *Chemosphere*, vol. 78, no. 5, pp. 569–575, 2010.

[25] A. Bhatnagar and I. Anastopoulos, "Adsorptive removal of bisphenol A (BPA) from aqueous solution: a review," *Chemosphere*, vol. 168, pp. 885–902, 2017.

[26] Y. Zhang, W. Cui, W. An, L. Liu, Y. Liang, and Y. Zhu, "Combination of photoelectrocatalysis and adsorption for removal of bisphenol A over TiO_2-graphene hydrogel with 3D network structure," *Applied Catalysis B: Environmental*, vol. 221, pp. 36–46, 2018.

[27] G. Y. S. Chan, J. Chang, T. A. Kurniawan, C.-X. Fu, H. Jiang, and Y. Je, "Removal of non-biodegradable compounds from stabilized leachate using VSEPRO membrane filtration," *Desalination*, vol. 202, no. 1-3, pp. 310–317, 2007.

[28] P. Wang, X. Zhou, Y. Zhang, L. Wang, K. Zhi, and Y. Jiang, "Synthesis and application of magnetic reduced graphene oxide composites for the removal of bisphenol A in aqueous solution—a mechanistic study," *RSC Advances*, vol. 6, no. 104, pp. 102348–102358, 2016.

[29] M. Vilve, S. Vilhunen, M. Vepsäläinen et al., "Degradation of 1,2-dichloroethane from wash water of ion-exchange resin using Fenton's oxidation," *Environmental Science and Pollution Research International*, vol. 17, no. 4, pp. 875–884, 2010.

[30] Z. Mengting, T. Kurniawan, Y. Yanping, R. Avtar, and M. Othman, "2D graphene oxide (GO) doped *p-n* type BiOI/-Bi_2WO_6 as a novel composite for photodegradation of bisphenol A (BPA) in aqueous solutions under UV-vis irradiation," *Materials Science and Engineering: C*, vol. 108, article 110420, 2020.

[31] Q. Wang, C. Yang, G. Zhang, L. Hu, and P. Wang, "Photocatalytic Fe-doped TiO_2/PSF composite UF membranes: characterization and performance on BPA removal under visible-light irradiation," *Chemical Engineering Journal*, vol. 319, pp. 39–47, 2017.

[32] H. Lan, G. Zhang, H. Zhang, H. Liu, R. Liu, and J. Qu, "Solvothermal synthesis of BiOI flower-like microspheres for efficient photocatalytic degradation of BPA under visible light irradiation," *Catalysis Communications*, vol. 98, pp. 9–12, 2017.

[33] A. Sivakumar, B. Murugesan, A. Loganathan, and P. Sivakumar, "A review on decolourisation of dyes by photodegradation using various bismuth catalysts," *Journal of the Taiwan Institute of Chemical Engineers*, vol. 45, no. 5, pp. 2300–2306, 2014.

[34] H. Xing, H. Ma, Y. Fu et al., "Preparation of g-C_3N_4/ZnO composites and their enhanced photocatalytic activity," *Materials Technology*, vol. 30, no. 2, pp. 122–127, 2015.

[35] S. J. Yang, J. H. Im, T. Kim, K. Lee, and C. R. Park, "MOF-derived ZnO and ZnO@C composites with high photocatalytic activity and adsorption capacity," *Journal of Hazardous Materials*, vol. 186, no. 1, pp. 376–382, 2011.

[36] T. Chang, Z. Li, G. Yun, Y. Jia, and H. Yang, "Enhanced photocatalytic activity of ZnO/CuO nanocomposites synthesized by hydrothermal method," *Nano-Micro Letters*, vol. 5, no. 3, pp. 163–168, 2013.

[37] H. A. Kiwaan, T. M. Atwee, E. A. Azab, and A. A. El-Bindary, "Efficient photocatalytic degradation of Acid Red 57 using synthesized ZnO nanowires," *Journal of the Chinese Chemical Society*, vol. 66, no. 1, pp. 89–98, 2019.

[38] S. Yang, P. Wu, M. Chen et al., "Enhanced photo-degradation of bisphenol a under simulated solar light irradiation by Zn–Ti mixed metal oxides loaded on graphene from aqueous media," *RSC Advances*, vol. 6, no. 32, pp. 26495–26504, 2016.

[39] C. Liu, M. Yue, L. Liu, Y. Rui, and W. Cui, "A separation-free 3D network ZnO/rGO–rGH hydrogel: adsorption enriched photocatalysis for environmental applications," *RSC Advances*, vol. 8, no. 40, pp. 22402–22410, 2018.

[40] S. S. Naik, S. J. Lee, T. Begildayeva, Y. Yu, H. Lee, and M. Y. Choi, "Pulsed laser synthesis of reduced graphene oxide supported ZnO/Au nanostructures in liquid with enhanced solar light photocatalytic activity," *Environmental Pollution*, vol. 266, article 115247, 2020.

[41] S. Kuriakose, V. Choudhary, B. Satpati, and S. Mohapatra, "Enhanced photocatalytic activity of Ag-ZnO hybrid plasmonic nanostructures prepared by a facile wet chemical method," *Beilstein Journal of Nanotechnology*, vol. 5, pp. 639–650, 2014.

[42] J. Lu, H. Wang, D. Peng, T. Chen, S. Dong, and Y. Chang, "Synthesis and properties of Au/ZnO nanorods as a plasmonic photocatalyst," *Physica E: Low-dimensional Systems and Nanostructures*, vol. 78, pp. 41–48, 2016.

[43] E. B. Choi and J.-H. Lee, "Dewetting behavior of Ag in Ag-coated Cu particle with thick Ag shell," *Applied Surface Science*, vol. 480, pp. 839–845, 2019.

[44] B. L. Martínez-Vargas, S. M. Durón-Torres, D. Bahena, J. L. Rodríguez-López, J. M. Peralta-Hernández, and A. Picos, "One-pot synthesis of ZnO–Ag and ZnO–Co nanohybrid materials for photocatalytic applications," *Journal of Physics and Chemistry of Solids*, vol. 135, article 109120, 2019.

[45] R. Anugrahwidya, N. Yudasari, and D. Tahir, "Optical and structural investigation of synthesis ZnO/Ag nanoparticles prepared by laser ablation in liquid," *Materials Science in Semiconductor Processing*, vol. 105, article 104712, 2020.

[46] P. Amornpitoksuk, S. Suwanboon, S. Sangkanu, A. Sukhoom, N. Muensit, and J. Baltrusaitis, "Synthesis, characterization, photocatalytic and antibacterial activities of Ag-doped ZnO powders modified with a diblock copolymer," *Powder Technology*, vol. 219, pp. 158–164, 2012.

[47] Ö. A. Yıldırım, H. E. Unalan, and C. Durucan, "Highly efficient room temperature synthesis of silver-doped zinc oxide (ZnO:Ag) nanoparticles: structural, optical, and photocatalytic properties," *Journal of the American Ceramic Society*, vol. 96, no. 3, pp. 766–773, 2013.

[48] A. C. Lucilha, M. R. . Silva, R. A. Ando, L. H. Dall'Antonia, and K. Takashima, "ZnO and Ag-ZnO crystals: synthesis, characterization, and application in heterogeneous photocatalysis," *Química Nova*, vol. 39, no. 4, pp. 409–414, 2016.

[49] V. H. Tran Thi, T. H. Cao, T. N. Pham, T. T. Pham, and M. C. Le, "Synergistic adsorption and photocatalytic activity under visible irradiation using Ag-ZnO/GO nanoparticles derived at low temperature," *Journal of Chemistry*, vol. 2019, Article ID 2979517, 13 pages, 2019.

[50] A. Kaur, G. Gupta, A. O. Ibhadon, D. B. Salunke, A. S. K. Sinha, and S. K. Kansal, "A facile synthesis of silver modified ZnO nanoplates for efficient removal of ofloxacin drug in aqueous phase under solar irradiation," *Journal of Environmental Chemical Engineering*, vol. 6, no. 3, pp. 3621–3630, 2018.

[51] W. Li, F. Hua, J. Yue, and J. Li, "Ag@AgCl plasmon-induced sensitized ZnO particle for high-efficiency photocatalytic property under visible light," *Applied Surface Science*, vol. 285, no. Part B, pp. 490–497, 2013.

[52] S.-i. Naya, T. Nikawa, K. Kimura, and H. Tada, "Rapid and complete removal of nonylphenol by gold nanoparticle/rutile titanium(IV) oxide plasmon photocatalyst," *ACS Catalysis*, vol. 3, no. 5, pp. 903–907, 2013.

[53] H. Liu, Y. Hu, Z. Zhang, X. Liu, H. Jia, and B. Xu, "Synthesis of spherical Ag/ZnO heterostructural composites with excellent photocatalytic activity under visible light and UV irradiation," *Applied Surface Science*, vol. 355, pp. 644–652, 2015.

[54] J. Y. C. Yang, Q. Li, and Y. Yu, "Facile synthesis of monodisperse porous ZnO nanospheres for organic pollutant degradation under simulated sunlight irradiation: the effect of operational parameters," *Materials Research Bulletin*, vol. 87, pp. 72–83, 2017.

[55] M. Behnajady, N. Modirshahla, and R. Hamzavi, "Kinetic study on photocatalytic degradation of C.I. Acid Yellow 23 by ZnO photocatalyst," *Journal of Hazardous Materials*, vol. 133, no. 1-3, pp. 226–232, 2006.

[56] A. Zyoud, A. Zu'bi, M. H. S. Helal, D. H. Park, G. Campet, and H. S. Hilal, "Optimizing photo-mineralization of aqueous methyl orange by nano-ZnO catalyst under simulated natural conditions," *Journal of Environmental Health Science & Engineering*, vol. 13, no. 1, 2015.

[57] X. Yang, Y. Li, Q. Du et al., "Highly effective removal of basic fuchsin from aqueous solutions by anionic polyacrylamide/-graphene oxide aerogels," *Journal of Colloid and Interface Science*, vol. 453, pp. 107–114, 2015.

[58] N. Lu, Y. Lu, F. Liu et al., "$H_3PW_{12}O_{40}/TiO_2$ catalyst-induced photodegradation of bisphenol A (BPA): kinetics, toxicity and degradation pathways," *Chemosphere*, vol. 91, no. 9, pp. 1266–1272, 2013.

[59] O. Bechambi, L. Jlaiel, W. Najjar, and S. Sayadi, "Photocatalytic degradation of bisphenol A in the presence of Ce–ZnO: evolution of kinetics, toxicity and photodegradation mechanism," *Materials Chemistry and Physics*, vol. 173, pp. 95–105, 2016.

[60] O. Bechambi, S. Sayadi, and W. Najjar, "Photocatalytic degradation of bisphenol A in the presence of C-doped ZnO: effect of operational parameters and photodegradation mechanism," *Journal of Industrial and Engineering Chemistry*, vol. 32, pp. 201–210, 2015.

[61] C. Chang, Y. Fu, M. Hu, C. Wang, G. Shan, and L. Zhu, "Photodegradation of bisphenol A by highly stable palladium-doped mesoporous graphite carbon nitride (Pd/mpg-C_3N_4) under simulated solar light irradiation," *Applied Catalysis B: Environmental*, vol. 142-143, pp. 553–560, 2013.

Hindawi
International Journal of Photoenergy
Volume 2020, Article ID 8868782, 7 pages
https://doi.org/10.1155/2020/8868782

Research Article

Microstructure Optimization of Mos_2/Sepiolite Nanocomposites via a Surfactant-Assisted Hydrothermal Strategy for High Efficiency Photocatalysis

Li Cui,[1,2] Ming Hao,[1,2] Fei Wang,[1,2] Baizeng Fang,[3] Jinsheng Liang,[1,2] Maomao Zhu,[1,2] and Xinlei Xie[1,2]

[1]*Key Laboratory of Special Functional Materials for Ecological Environment and Information (Hebei University of Technology), Ministry of Education, Tianjin 300130, China*
[2]*Institute of Power Source and Ecomaterials Science, Hebei University of Technology, Tianjin 300130, China*
[3]*Department of Chemical & Biological Engineering, University of British Columbia, Vancouver, Canada V6T 1Z3*

Correspondence should be addressed to Fei Wang; wangfei@hebut.edu.cn

Received 27 May 2020; Revised 21 June 2020; Accepted 30 June 2020; Published 18 July 2020

Academic Editor: Hao Li

The unique structure of two-dimensional molybdenum disulfide (MoS_2) with rich active sites makes it a promising catalyst, whereas it also brings structural instability. Surfactant-assisted synthesis of MoS_2 can be regarded as a simple way to regulate the microstructure. In this work, the surfactant additives were adopted to optimize the microstructure of MoS_2/sepiolite nanocomposite, and the effects of surfactants type and concentration were investigated. For the sample prepared with 1 mol/L sodium dodecyl benzene sulfonate (SDBS), it exhibits the highest intensity for the peak of MoS_2 at 14.2°, highly dispersed MoS_2 nanosheet on the sepiolite, the lowest absorption intensity of Rhodamine B (RhB) at 553 nm of the wavelength, and the highest photocatalytic activity which is 2.5 times and 4.2 times higher than those prepared with 1 mol/L hexadecyl trimethyl ammonium bromide (CTAB) and 1 mol/L polyvinyl pyrrolidone (PVP) after a 150-minute irradiation, respectively. The above results suggest SDBS is the optimal surfactant to optimize the microstructure of MoS_2/sepiolite nanocomposite. This work could provide new insights into the fabrication of high-quality MoS_2-based nanocomposite.

1. Introduction

As a typical two-dimensional (2D) semiconducting material, MoS_2 with a typical layered structure is formed by stacking of planes. Each plane consists of covalently bonded S-Mo-S atoms in close-packed hexagonal structure, and adjacent planes are held together by van der Waals interactions. MoS_2 has gradually aroused particular interest and enormous attention due to its unique structure which endows MoS_2 with excellent properties for various applications, including photocatalysts [1–3], electrocatalysts [4], supercapacitors [5], sensors [6], and lubricants [7]. However, the high specific surface energy makes it easy agglomeration which results in the decrease of active sites and edges [8]. In order to combat these drawbacks, researchers put their effort to increase the dispersion as well as reduce the layer numbers of MoS_2 nanosheets through different strategies, such as adopting a carrier [9] and taking atomic layer deposition [10]. Nevertheless, the high cost and complex method of preparation restrict them to broad application. In fact, the surfactant-assisted synthesis of MoS_2 has the advantages of low cost, easy operation, and excellent performance, and some surfactants are utilized to optimize MoS_2-based nanocomposite [11–15]. Sepiolite is a typical clay mineral with the features of environment-friendly and low cost, which makes it a good carrier for catalyst because the large surface specific area and excellent adsorption are benefit for the high catalytic performance [16–19]. However, surfactant (cationic, anionic, and non-ionic surfactant) with different charges will affect both catalyst and carrier, due to the surface charge of sepiolite [20, 21]. To date, only few researches have focused on the influences of surfactant on MoS_2 supported by mineral carriers.

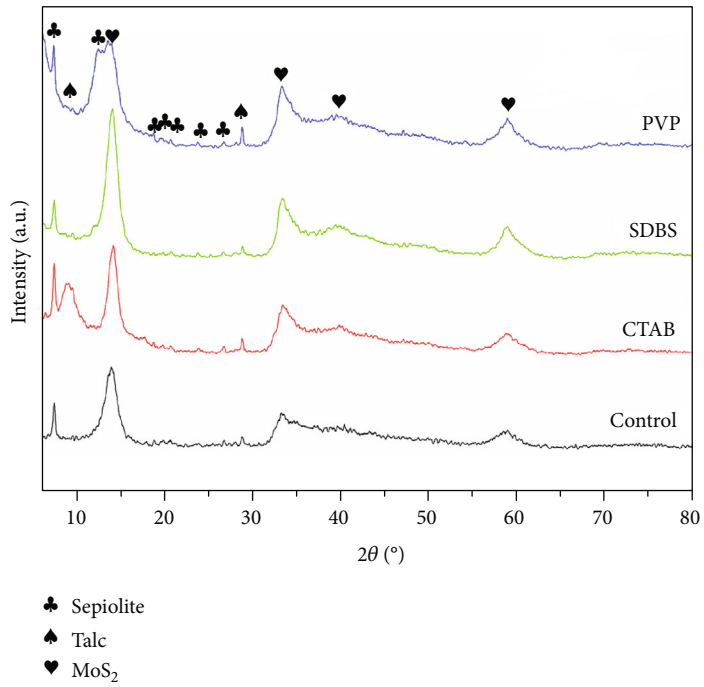

Figure 1: XRD patterns of the samples prepared with different surfactants.

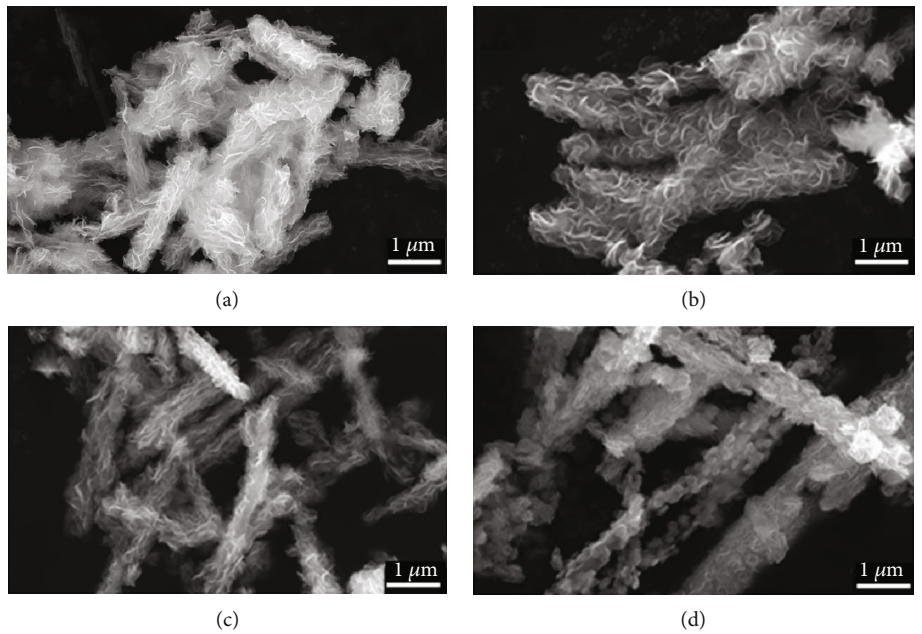

Figure 2: SEM images of the samples prepared with different surfactants. (a) Control; (b) CTAB; (c) SDBS; (d) PVP.

In the previous study, we have found the excellent performance of composites *via*adopting minerals [22–24]. Subsequently, we succeeded in fabricating natural SEP bulks into nano-sized fibers using high-speed airflow techniques [25] and utilized them to achieve the agglomeration decrease of catalysts [26]. Moreover, we also have prepared MoS_2/sepiolite nanocomposite via a microwave hydrothermal method [27]. In this study, the surfactant additives were used to optimize the microstructure of MoS_2/sepiolite nanocomposite, and the effects of surfactants type and concentration were also investigated. This work is believed to offer a new strategy for preparing high-quality MoS_2-based catalyst.

2. Experimental

2.1. Materials. The sepiolite was purchased from Hebei Province, China. All chemical reagents were purchased from Tianjin Damao Chemical Co., Ltd., without further purified.

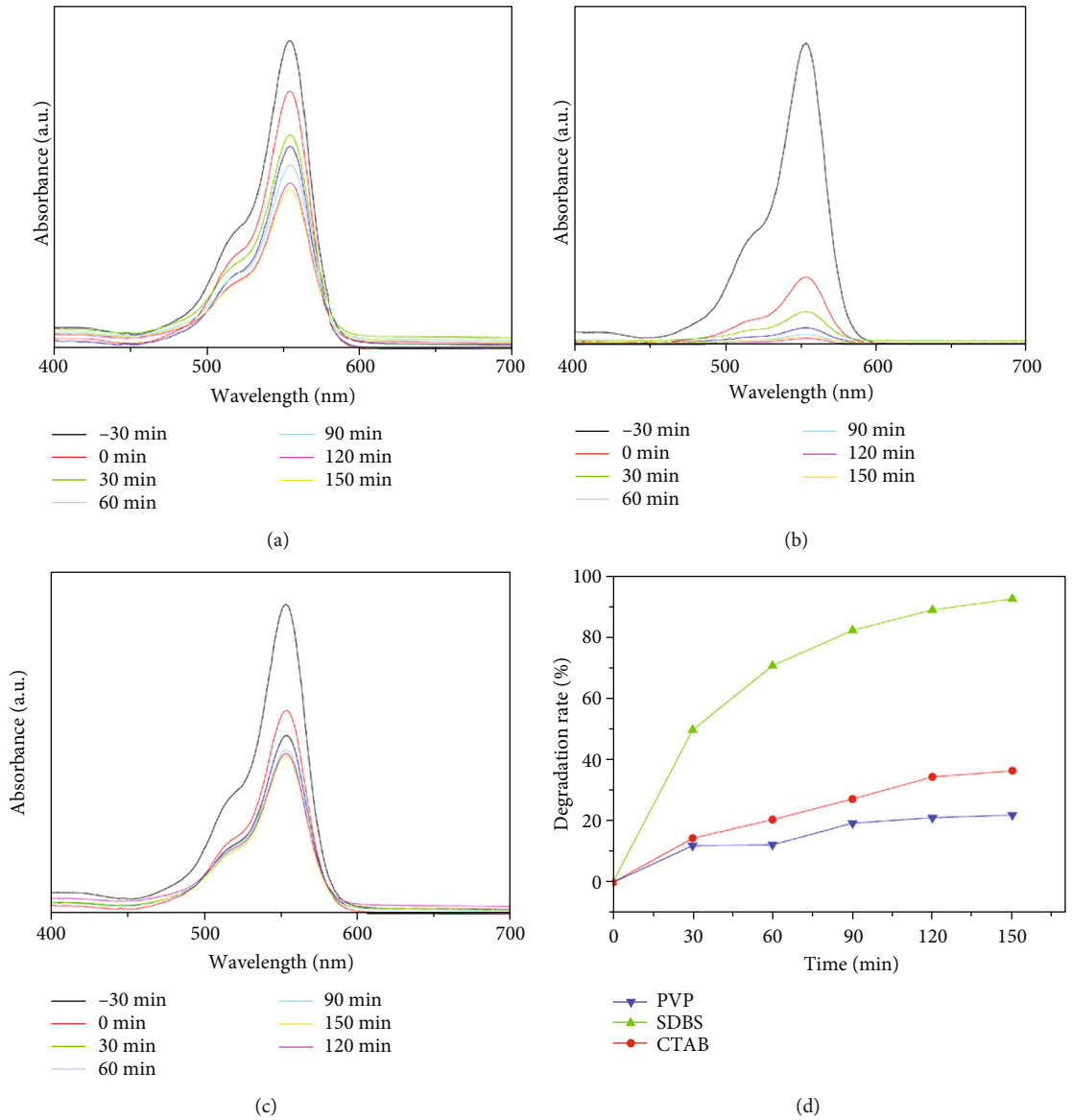

Figure 3: Ultraviolet visible absorption spectra and photocatalysis performance of the samples prepared with different surfactants: (a) CTAB; (b) SDBS; (c) PVP; (d) photocatalytic performance for RhB degradation.

2.2. Sample Preparation. The samples were fabricated by a surfactant-assisted hydrothermal method, and the experimental procedures are similar to reference [27]. In brief, 2 mmol of $(NH_4)_6Mo_7O_{24}{\cdot}4H_2O$, 30 mmol of CH_4N_2S, and appropriate dosage of a certain kind of surfactant (CTAB, SDBS and PVP, respectively) with suitable concentration were dissolved in 70 mL of deionized water and stirred for 30 min. Then, 0.6 g of sepiolite nanofiber powders prepared *via* high-speed airflow techniques [25] for the natural SEP bulks were added into the solution and kept stirring for another 0.5 h. Next, the mixture was sonicated for 10 min. After that, 50 mL of the above suspension was transferred to a 100 mL Teflon-lined stainless steel autoclave and kept at 220°C for 3 h under microwave heating. After the samples were cooled down to room temperature, the final products were obtained by filtration, washed several times with deionized water, and dried in the vacuum oven at 80°C for 12 h.

2.3. Characterization and Performance Tests. X-ray powder diffraction (XRD) was performed by a D8 ADVANCE X-ray diffractometer with nickel-filtered ($V = 40$ kV, $I = 40$ mA) Cu Kα radiation as the X-ray source ($\lambda = 1.54$ Å). The morphologies of the as-synthesized samples were observed by SEM (FEI Nano SEM450) under an accelerating voltage of 1.00 kV.

The photocatalytic activity of the as-prepared samples was tested through the photocatalytic degradation of RhB under visible light irradiation. 20 mg of samples were dispersed into 100 mL of RhB solution (20 mg/L), stirring the produced suspension in the dark for 30 min to reach the adsorption/desorption equilibrium. The suspension was subjected to irradiation by a 500 W Xe lamp ($\lambda > 420$ nm) under stirring at ambient conditions. After 30 min, 6 mL of the suspension was taken out and centrifuged to remove the photocatalysts. The filtrates were analyzed through recording the

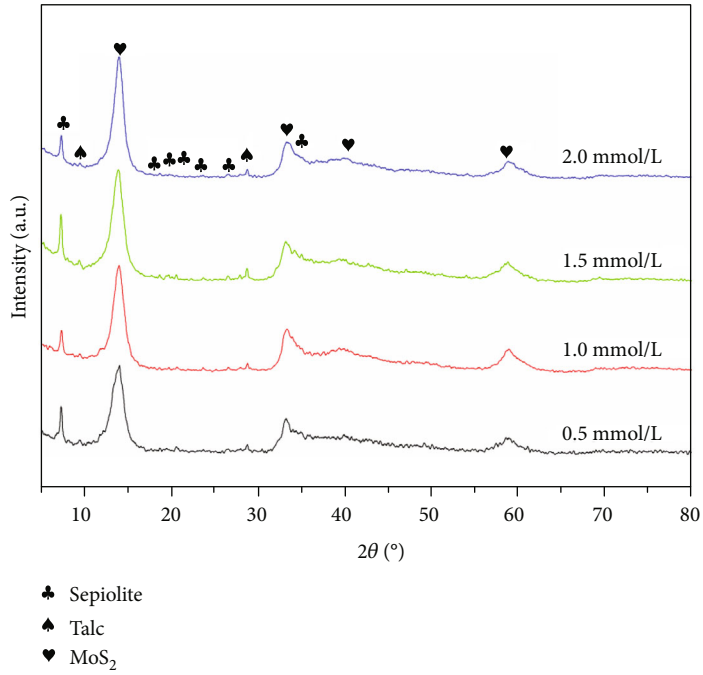

Figure 4: XRD patterns of the samples prepared with different concentration of SDBS.

UV-Vis spectra by a Shimadzu UV-1800 spectrophotometer. The calculated method of photodegradation efficiency was shown in equation (1) where D represents the photodegradation efficiency of catalyst, A_0 represents the absorbance value at the beginning of illumination, and A_t represents the absorbance value at a certain time t of illumination.

$$D(\%) = (A_0 - A_t)/A_0. \quad (1)$$

3. Results and Discussion

Figure 1 shows the XRD patterns of the samples prepared with different surfactants. The two main phases are sepiolite and 2H-MoS_2 which are unchanged, indicating the structure of nanocomposite kept stable after adding surfactant [28, 29]. Compared with the control sample, surfactant-assisted synthesis of nanocomposite exhibits sharper peaks of MoS_2 (101) and (110) facets at 33.5° and 58.3°, respectively, which suggests the better crystallinity of MoS_2. Meanwhile, the sample prepared with SDBS shows the highest intensity for the peak of MoS_2 (002) facet at 14.2°, suggesting the increased content of MoS_2 [30]. Besides, the sample prepared by the similar process coupled with PVP or CTAB has almost no influence on the MoS_2 phase in nanocomposite.

SEM images directly show the morphology of sample prepared with different surfactants (Figure 2). Sample prepared with PVP suffers from serious agglomeration where MoS_2 nanosheets transferred to a microsphere morphology contrast to the control sample (Figures 2(a) and 2(d)), while MoS_2 in nanocomposite remains the good dispersion when CTAB or SDBS are added (Figures 2(b) and 2(c)). The sample morphology suggests that PVP is not suitable to optimize the MoS_2 supported by sepiolite.

To further identify the optimal surfactant, photocatalytic degradation of RhB is adopted as a probe reaction. As shown in Figure 3, the absorbance of RhB for all samples decreased at the maximum absorption wavelength along with the increase of lighting time. However, the sample prepared with SDBS has the maximum descent, compared with those used CTAB and PVP after a 150-minute irradiation (Figures 3(a)–3(c)). Moreover, the degradation efficiency of RhB for the sample prepared with SDBS reaches about 93% after irradiation of 150 minutes (Figure 3(d)), which is much higher than those prepared with CTAB (37%) and PVP (22%). Combined with the results of XRD, SEM, and photocatalysis performance, SDBS can be identified as the optimal surfactant.

The most suitable concentration of the SDBS is studied subsequently. As shown in Figure 4, the samples prepared with 1 mol/L and 1.5 mol/L SDBS show the sharper peaks of MoS_2 (101) and (110) facets at 33.5° and 58.3°, respectively, which indicates the appropriate concentration of SDBS can increased crystallinity of MoS_2 in nanocomposite while sample prepared with too high (2 mol/L) or low (0.5 mol/L) concentration of SDBS is unsuitable.

Figure 5 shows the morphology of the samples prepared with different concentration of SDBS. It can be seen that MoS_2 in nanocomposite remains the architecture of nanosheet and disperses on the sepiolite surface, but the MoS_2 on the surface of sepiolite disperses sparsely when the concentration is 0.5 mol/L (Figure 5(a)). When the concentration comes up to 1.5 mol/L and 2 mol/L, a few parts of MoS_2 suffer from slight agglomeration (Figures 5(c) and 5(d)). When the concentration is 1 mol/L, the MoS_2 nanosheets are uniformly dispersed on the sepiolite surface with the high density and no obvious agglomeration (Figure 5(b)). Consequently, the concentration of SDBS has

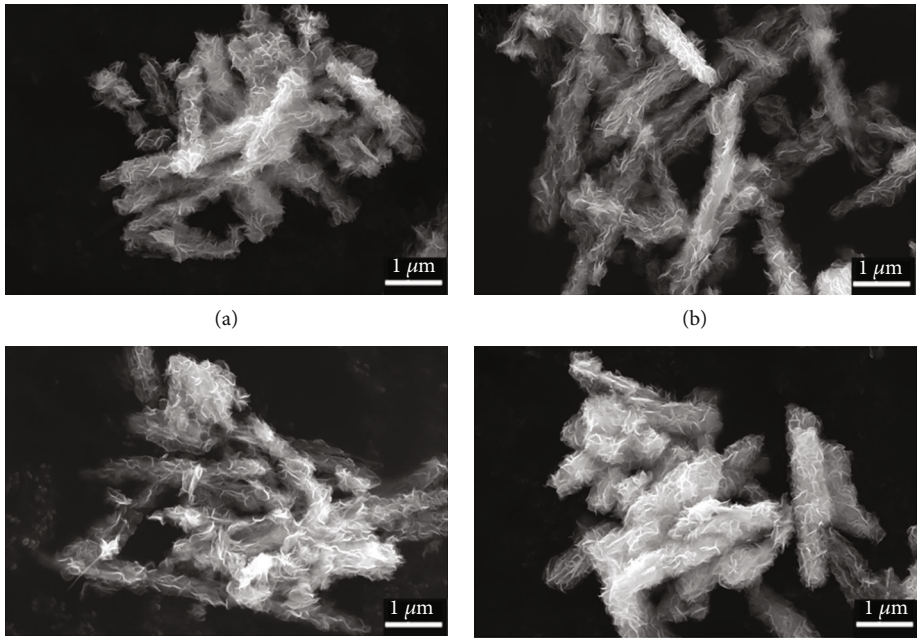

Figure 5: SEM images of the samples prepared with different concentration of SDBS. (a) 0.5 mmol/L; (b) 1.0 mmol/L; (c) 1.5 mmol/L; (d) 2.0 mmol/L.

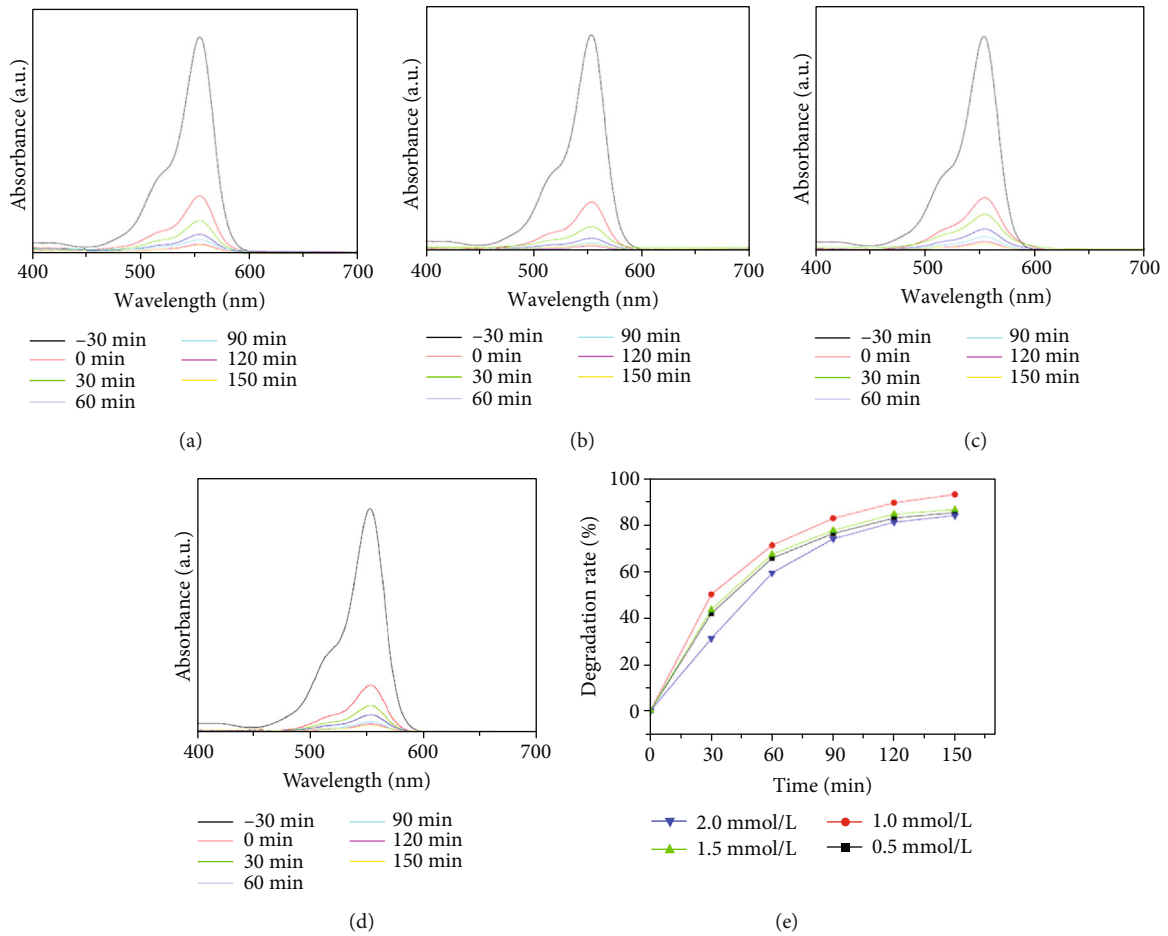

Figure 6: Ultraviolet visible absorption spectra and photocatalysis performance of the sample prepared with different concentration of SDBS. (a) 0.5 mmol/L; (b) 1.0 mmol/L; (c) 1.5 mmol/L; (d) 2.0 mmol/L; (e) photocatalytic performance for RhB degradation.

obvious influence on the dispersion of MoS_2 in the nanocomposite.

The ultraviolet visible absorption spectra and photocatalytic performance of the samples prepared with different concentration of SDBS are also studied to find the optimal condition (Figure 6). The sample prepared with 1 mol/L SDBS has the maximum descent for the absorbance of RhB compared with those used other concentrations (Figures 6(a)–6(d)). In addition, photocatalytic activity of samples toward RhB degradation can be as an important evidence to obtain the optimal concentration of SDBS, and the RhB degradation efficiency of the sample prepared with 1 mol/L SDBS is the highest (Figure 6(e)). Thus, the optimal concentration of SDBS can be identified as 1 mol/L.

4. Conclusions

In summary, MoS_2/sepiolite nanocomposite was optimized via a surfactant-assisted hydrothermal method, and the influence of surfactants type and concentration was also studied. The results show that the photocatalysis activity of the nanocomposite prepared with 1 mol/L SDBS as the optimal condition toward RhB degradation reaches about 93%, which is extremely higher than those used CTAB and PVP with the same concentration. SEM images directly show the microsphere MoS_2 suffering from serious agglomeration when using PVP. Meanwhile, the increased content of $MoS_2$is exhibited with the present of SDBS. Among the sample prepared with different concentrations of SDBS, 1 mol/L SDBS as the optimal concentration makes the best crystallinity of MoS_2 in nanocomposite. This work provides a new perspective for regulating the microstructure of MoS_2-based catalyst.

Data Availability

The manuscript contains all of the data.

Conflicts of Interest

There is no conflict interest to declare.

Authors' Contributions

Li Cui and Ming Hao contributed equally to this work.

Acknowledgments

This work was financially supported by the National Natural Science Foundation of China (No. 51874115), Introduced Overseas Scholars Program of Hebei Province, China (No. C201808), Enterprise Science and Technology Commissioner Project of Tianjin City, China (No. 19JCTPJC56100), and Excellent Young Scientist Foundation of Hebei Province, China (No. E2018202241).

References

[1] Z. Wu, X. He, Y. Xue et al., "Cyclodextrins grafted MoS_2/g-C_3N_4 as high-performance photocatalysts for the removal of glyphosate and Cr (VI) from simulated agricultural runoff," *Chemical Engineering Journal*, vol. 399, p. 125747, 2020.

[2] B. Chen, Y. Meng, J. Sha, C. Zhong, W. Hu, and N. Zhao, "Preparation of MoS_2/TiO_2 based nanocomposites for photocatalysis and rechargeable batteries: progress, challenges, and perspective," *Nanoscale*, vol. 10, no. 1, pp. 34–68, 2018.

[3] H. He, J. Lin, W. Fu et al., "MoS_2/TiO_2 edge-on heterostructure for efficient photocatalytic hydrogen evolution," *Advanced Energy Materials*, vol. 6, no. 14, p. 1600464, 2016.

[4] Y. Yang, K. Zhang, H. Lin et al., "MoS_2–Ni_3S_2 heteronanorods as efficient and stable bifunctional electrocatalysts for overall water splitting," *ACS Catalysis*, vol. 7, no. 4, pp. 2357–2366, 2017.

[5] H. Tang, J. Wang, H. Yin, H. Zhao, D. Wang, and Z. Tang, "Growth of polypyrrole ultrathin films on MoS_2 monolayers as high-performance supercapacitor electrodes," *Advanced Materials*, vol. 27, no. 6, pp. 1117–1123, 2015.

[6] S. Y. Park, J. E. Lee, Y. H. Kim et al., "Room temperature humidity sensors based on rGO/MoS_2 hybrid composites synthesized by hydrothermal method," *Sensors and Actuators B-chemical*, vol. 258, pp. 775–782, 2018.

[7] H. Xie, B. Jiang, J. He, X. Xia, and F. Pan, "Lubrication performance of MoS_2 and SiO_2 nanoparticles as lubricant additives in magnesium alloy-steel contacts," *Tribology International*, vol. 93, pp. 63–70, 2016.

[8] J. Zhou, M. Guo, L. Wang et al., "1T-MoS_2 nanosheets confined among TiO_2 nanotube arrays for high performance supercapacitor," *Chemical Engineering Journal*, vol. 366, pp. 163–171, 2019.

[9] D. Sun, D. Ye, P. Liu et al., "MoS_2/graphene nanosheets from commercial bulky MoS_2 and graphite as anode materials for high rate sodium-ion batteries," *Advanced Energy Materials*, vol. 8, no. 10, p. 1702383, 2018.

[10] J. Yang and L. Liu, "Trickle flow aided atomic layer deposition (ALD) strategy for ultrathin molybdenum disulfide (MoS_2) synthesis," *ACS Applied Materials & Interfaces*, vol. 11, no. 39, pp. 36270–36277, 2019.

[11] M. Li, D. Wang, J. Li et al., "Surfactant-assisted hydrothermally synthesized MoS_2 samples with controllable morphologies and structures for anthracene hydrogenation," *Chinese Journal of Catalysis*, vol. 38, no. 3, pp. 597–606, 2017.

[12] Y. Zhang, W. Zeng, and Y. Li, "The hydrothermal synthesis of 3D hierarchical porous MoS_2 microspheres assembled by nanosheets with excellent gas sensing properties," *Journal of Alloys and Compounds*, vol. 749, no. 15, pp. 355–362, 2018.

[13] S. Kumari, R. Gusain, N. Kumar, and O. P. Khatri, "PEG-mediated hydrothermal synthesis of hierarchical microspheres of MoS_2 nanosheets and their potential for lubrication application," *Journal of Industrial and Engineering Chemistry*, vol. 42, pp. 87–94, 2016.

[14] X. Zeng and W. Qin, "Synthesis of MoS_2 nanoparticles using MoO_3 nanobelts as precursor via a PVP-assisted hydrothermal method," *Materials Letters*, vol. 182, pp. 347–350, 2016.

[15] A. Trenczekzajac, J. Banas, and M. Radecka, "Photoactive TiO_2/MoS_2 electrode with prolonged stability," *International Journal of Hydrogen Energy*, vol. 43, no. 14, pp. 6824–6837, 2018.

[16] H. Li, W. Chai, and G. Henkelman, "Selectivity for ethanol partial oxidation: the unique chemistry of single-atom alloy catalysts on Au, Ag, and Cu (111)," *Journal of Materials Chemistry A*, vol. 7, no. 41, pp. 23868–23877, 2019.

[17] Y. Piao, Q. Jiang, H. Li et al., "Identify Zr promotion effects in atomic scale for Co-based catalysts in Fischer-Tropsch synthesis," *ACS Catalysis*, vol. 10, pp. 7894–7906, 2020.

[18] X. Hu, Z. Sun, J. Song, G. Zhang, C. Li, and S. Zheng, "Synthesis of novel ternary heterogeneous BiOCl/TiO_2/sepiolite composite with enhanced visible-light-induced photocatalytic activity towards tetracycline," *Journal of Colloid and Interface Science*, vol. 533, pp. 238–250, 2019.

[19] H. Li, S. Guo, K. Shin, M. S. Wong, and G. Henkelman, "Design of a Pd-Au nitrite reduction catalyst by identifying and optimizing active ensembles," *ACS Catalysis*, vol. 9, no. 9, pp. 7957–7966, 2019.

[20] F. Wang, M. Hao, J. Liang et al., "A facile fabrication of sepiolite mineral nanofibers with excellent adsorption performance for Cd^{2+} ions," *RSC Advances*, vol. 9, no. 69, pp. 40184–40189, 2019.

[21] J. A. Carmona, P. Ramírez, L. A. Trujillo-Cayado, A. Caro, and J. Muñoz, "Rheological and microstructural properties of sepiolite gels. Influence of the addition of ionic surfactants," *Journal of Industrial and Engineering Chemistry*, vol. 59, pp. 1–7, 2018.

[22] F. Wang, P. Gao, J. Liang et al., "A novel and simple microwave hydrothermal method for preparation of $CoAl_2O_4$/sepiolite nanofibers composite," *Ceramics International*, vol. 45, no. 18, pp. 24923–24926, 2019.

[23] Q. Tang, F. Wang, X. Liu et al., "Surface modified palygorskite nanofibers and their applications as reinforcement phase in cis-polybutadiene rubber nanocomposites," *Applied Clay Science*, vol. 132-133, pp. 175–181, 2016.

[24] F. Wang, Z. Xie, J. Liang et al., "Tourmaline-modified FeMn-TiO_x catalysts for improved low-temperature NH_3-SCR performance," *Environmental Science & Technology*, vol. 53, no. 12, pp. 6989–6996, 2019.

[25] J. Liang, F. Wang, Q. Tang et al., "A method of preparing mineral nanofiber," 2009, CN 200910070297.8.

[26] T. Zhang, F. Wang, J. Liang et al., "A novel and facile impregnation-combustion fabrication of spherical $CoAl_2O_4$ supported on sepiolite nanofibers," *Ceramics International*, vol. 44, no. 16, pp. 19543–19546, 2018.

[27] F. Wang, M. Zhu, J. Liang et al., "Preparation method of MoS_2-sepiolite nanofiber composite," 2018, CN 201810359072.3.

[28] Y. Zhang, L. Wang, F. Wang, J. Liang, S. Ran, and J. Sun, "Phase transformation and morphology evolution of sepiolite fibers during thermal treatment," *Applied Clay Science*, vol. 143, pp. 205–211, 2017.

[29] S. Karunakaran, S. Pandit, B. Basu, and M. de, "Simultaneous exfoliation and functionalization of 2H-MoS_2 by thiolated surfactants: applications in enhanced antibacterial activity," *Journal of the American Chemical Society*, vol. 140, no. 39, pp. 12634–12644, 2018.

[30] D. Wang, Y. Xu, F. Sun, Q. Zhang, P. Wang, and X. Wang, "Enhanced photocatalytic activity of TiO_2 under sunlight by MoS_2 nanodots modification," *Applied Surface Science*, vol. 377, pp. 221–227, 2016.